Predictability of Stratified Turbulence

by

Martín F. Díaz Robles

A thesis
presented to the University of Waterloo
in fulfillment of the
thesis requirement for the degree of
Master of Mathematics
in
Applied Mathematics

Waterloo, Ontario, Canada, 2023

Author's Declaration

I hereby declare that I am the sole author of this thesis. This is a true copy of the thesis, including any required final revisions, as accepted by my examiners.

I understand that my thesis may be made electronically available to the public.

Abstract

In the study of geophysical fluid dynamics, predictability of dynamics at different scales still stands in the foreground of interest as one of the primary challenges. Following Lorenz's pioneering framework, several results from homogeneous and isotropic turbulence have suggested that flows with many scales of motion present limited predictability due to the inevitable contamination of error from small to large scales, even if initially confined to small scales. In this work, we investigate the predictability of freely decaying stratified turbulence, which is representative of small-scale geophysical turbulence where rotational effects are neglected.

Predictability of stratified turbulence is studied using direct numerical simulations by analyzing the error growth in pairs of realizations of velocity fields departing from almost identical initial conditions. Previous studies have indicated that the finite range of predictability is determined by the slope of the flow's kinetic energy spectrum. In stratified turbulence, the shape of the energy spectrum depends on the buoyancy Reynolds number Re_b, at least when Re_b is not too large. We perform a comparative analysis of spectra and perturbation upscale growth behaviour in different regimes of stratified turbulence from $\mathcal{O}(10)$ to unitary order of buoyancy Reynolds number.

Furthermore, we explore the sensitivity of our experimental outcomes with respect to error introduction. There were no discernible changes between the behavior of the systems and their associated error dynamics while modifying the geometrical shape of the error introduction, going from a spherical domain complement to a cylindrical complement. Likewise, the experiments were insensitive to adjusting the cutoff wavenumber k_c at which the error is introduced while keeping the same initial error kinetic energy, obtaining similar results for $k_c \in \{20, 40, 60, 80\}$.

Acknowledgements

Por el gis: Joven Páez y Mike.
Por el juego: Ponchito, Juliette, Rick y Sina.
Por la sangre: James, James Jr. y Albert.
Y por el tiempo: Gaby.

Gracias.[1]

[1]Vocabulary list: gis = chalk, juego = game, sangre = blood, tiempo = time, Gracias = Thanks. The rest of the words are names, pronouns and connectors.

Dedication

To Mini and Coco.

Table of Contents

List of Figures

List of Tables

Chapter I

Introduction

> You must study turbulence Martin. The study of turbulence is the perfect type of a perfect pleasure. It is exquisite, and it leaves one unsatisfied. What more can one want?
>
> (*paraphrased*) *Michael Waite*

I.1 Turbulence

Hauntingly beautiful, that would be the best description that the author of this text could ever give to such a phenomenon, which beyond requiring a sterile understanding, demands above all aesthetic admiration. As we profess much respect and affection to our subject of study, we will be reluctant to adopt the fearful and unfortunately predominant position to avoid giving a definition to the concept of turbulence for the sake of not disturbing certain areas of the scientific community. Conversely, in order to do it justice and provide a decent definition it is necessary to first take a step back and identify the principal characteristics that outline its phenomenology.

It is the author's strong believe that the subject of turbulence could not be first approached in any other way than from real life experiences. Hence, in

an exercise that aims to bottle up in the context of fluid dynamics framework the grace and beauty of the phenomenon that we perceive with our eyes, we will discuss the properties and origins of turbulence starting each time with the illustrative nature of an example.

- *Randomness:* Whether we are admiring the dance generated by the smoke of a cigarette, or the flow of water in a river after it meets a rock, turbulence always arises in an erratic manner. Certainly, when we are analysing the motion of real fluids, it may seem that turbulence encapsulates that inevitable tendency of disrupting any kind of stable or laminar flow. This is translated experimentally in the incapacity to replicate in two different occasions the exact same turbulent flow.

  With that in mind, it is natural to assess that the velocity field of a turbulent flow presents large spatial and temporal fluctuations and, as an immediate consequence, our capacity for predictability under these condition would always be limited. The origin of this feature may be puzzling at first glance; if we think that at the end it is just a macroscopic phenomenon subject to classical continuum mechanics interactions and described by deterministic equations such as Navier-Stokes (or one of their multiple sub-versions), where does the chaotic or random behavior come from?

  The answer to the previous question is usually attributed to the presence of the *advective* term inside the Navier-Stokes equations:

$$\frac{\partial \mathbf{u}}{\partial t} + \underbrace{(\mathbf{u} \cdot \nabla \mathbf{u})}_{\text{advective term}} = -\nabla p + \nu \nabla^2 \mathbf{u}, \tag{I.1}$$

  where $\mathbf{u}$ is the velocity field, p and ν are the kinematic pressure and viscosity respectively. In this introductory discussion of turbulence, we are assuming constant density, but buoyancy and stratification will be incorporated below. As pointed out by Davidson (2004)[1], it is rather frequent to find that non-linear differential equations present extreme sensitivity to initial conditions giving place to a chaotic regime; in fact,

[1] It is worth noting that even though this work primarily relies on primary sources, textbooks have also been cited as they provide a concise and organized context.

the origin of turbulence may be regarded as the consequence of an *infinite sequence of bifurcations* (Landau, 1944), each of them adding random components to the velocity field. The reason why turbulence is not commonly approached within the context of complex system theory is because of the near-infinite and strongly coupled degrees of freedom that the problem possess.

On the other hand, the random nature of turbulence instinctively leads to the need for a statistical treatment, which consists of decomposing the velocity field into a characteristic mean flow and the contributions of turbulent (stochastic) fluctuations. Much of the study of turbulence could be summarized as the attempt to understand the statistical correlation of turbulent fluctuations between two different points in space and the endeavor to solve the closure problems that arise from it.

Finally, it is important to note that, regardless of the fact that the Navier-Stokes equation basically encapsulates the essence of Newton's second law for a lump of fluid, a huge difference is that the former one is *not* time-reversible (Davidson, 2004).

- *Range of scales*: From the air exhaled by my supervisor's lungs to the rage of the wind in a storm, turbulence seems to be a phenomenon that spans a wide range of scales. This broad spectrum of motion gives turbulence some kind of universality but still certain conditions must be fulfilled in order to have it. As Reynolds (1883) famously addressed with his study on the conditions in which the flow of fluid in pipes transitioned from laminar flow to turbulent flow, it is necessary to have a "sufficiently high" Reynolds number, which is a dimensionless parameter that quantifies the ratio between the inertial and viscous forces of a fluid, being defined as

$$\mathrm{Re} = \frac{uL}{\nu}, \tag{I.2}$$

where L and u are, respectively, the characteristic length and velocity. Therefore, fluids with higher viscosity but regular velocities and characteristic lengths tend to be less turbulent. That is the reason why it is so difficult to generate turbulence when playing with maple syrup over the kitchen table.

- *Mixing nature:* Everyone who enjoys drinking coffee with cream or adds milk to their tea will be familiar with the extraordinary capacity that turbulent flows possess for mixing momentum, heat and other types of scalars. The prevalence of agitations due to the fluctuations of the velocity field give turbulence a great efficiency for distributing the components of a fluid. This turbulent diffusion depends entirely on the flow conditions, but it is not a property of the fluid itself.

  In a similar note, turbulent flow tends to be associated with the concept of dissipation, nonetheless we have to be meticulous and notice that the presence of viscosity is the one responsible for the dissipative quality of any type of flow, not just turbulent flow. In regions of the space where the instantaneous gradient of velocity is particularly large, the shear stress within a fluid would be great as well, giving way to a pronounced dissipation of energy.

- *Vorticity:* It is hard to find someone who is not immediately hypnotized by the majesty of Jupiter's atmosphere, or at least point out with intrigue how its great red spot stands out just below the northern hemisphere. This example leads us to one of the most essential features of turbulence, the presence of vorticity ($\boldsymbol{\omega} = \nabla \times \mathbf{u}$). As expressed by Davidson (2004) and Lesieur (2014) there are great advantages on working directly with the vorticity field, beginning with a relatively simpler governing equation

$$\frac{D\boldsymbol{\omega}}{Dt} = (\boldsymbol{\omega} \cdot \nabla)\mathbf{u} + \nu\nabla^2\boldsymbol{\omega}, \tag{I.3}$$

  again assuming constant density and flow. Furthermore, the dynamics of vorticity provide us with useful tools for describing the constitution and evolution of turbulent flows such as vortex tubes and vortex stretching. As stated by Lesieur (2014) turbulence can be regarded as *a collection of thin vortex tubes stretched by the induced velocity field* as shown in Figure I.1. This vortex-tube stretching might lead to the formation of regions of space characterized by a high vorticity surrounded by regions of low vorticity, corresponding to the intermittency that we observe frequently in turbulent flows. In fact, coming back to the energy distribution topic, it is believed that dissipation occurs due to the action

of viscosity on the smaller vortices created by vortex stretching which transfers energy to smaller scales from the larger ones.

Figure I.1: Turbulence as a tangle of vortical structures.

This is a good moment to remark that most of the literature use the term "eddy" to a fault in order to ascribe nearly anything related with turbulence. The main problem about this term is that, in practice, it can draw a misleading picture that reduces the "spinning nature" of vorticity to whirlpool-like arrangements [2], when the topology of vortical structures can be far more intricate (and interesting!). Hence, for the means of this work we will avoid confusion using instead *blobs of vorticity* (or "blovs" for short) to refer to those vortical structures (vortices sheets, rings, tubes, etc.) of different sizes that predominate within turbulent flows.

Gathering the fore description and analysis of turbulence we can finally present the next:

Definition I.1.1. Incompressible *turbulence* is a spatially complex distribution of vorticity which evolve in a random manner in accordance to equation I.3, resulting from a fluid flow on a high Reynolds number regime. The vorticity field is stochastic in both time and space, and exhibits a vast and continuous distribution of length and time scales as well as intermittency.[3]

[2] The very etymology of the word *eddy* points to that fact: from ed- ("turning, back, reverse") + ēa ("water").

[3] This should not be taken as a mathematical definition, but as a formal and well rounded definition nonetheless.

I.1.1 Energy cascade: Kolmogorov-Obukhov theory

As turbulence is characterized by a wide range of scales of motion (gracefully described by definition I.1.1), an almost instinctive question arises when we ask ourselves if there is any particular way of interaction between the different scales of motion on a turbulent flow or, to be more precise, how exactly is the distribution and transfer of energy across all those scales?

We can infer that the largest blovs, due to the amount of mass and associated larger velocity, contain most of the kinetic energy in a turbulent system. We also know that three dimensional vortical structures tend to change in size primarily through vortex stretching. If we imagine the spatial coexistence of different sized blovs, it is natural to think that there should be some kind of interaction between them. At this point it is customary to resort to the poetic abilities of L.F. Richardson[4], and postulate a cartoon where the *main* energy interaction amidst blovs occurs when they have *similar sizes*. Therefore, it is thought that the kinetic energy of a turbulent flow is continually passed down from large scale blovs to smaller ones. This multi-step process or *cascade* is principally driven by inertial forces due to the strain field stretching and deforming blovs as marked out by Davidson (2004).

Now, in order to acknowledge the dissipative nature of turbulence, it is necessary to relate the end of this cascade with the role of viscosity, damping away turbulence at small scales. With this in mind, a reasonable hypothesis would be that the smallest possible length scale of blovs (η) would *just* be a function of viscosity (ν) and viscous dissipation of kinetic energy per unit of mass ($\epsilon = 2\nu\langle s_{ij}s_{ij}\rangle$ where s_{ij} is the strain rate tensor and we are averaging over the entire domain). In 1941, using the previous hypothesis and stratagem of dimensional analysis, A.N. Kolmogorov (1941) proposed that

$$\eta \sim \left(\frac{\nu^3}{\epsilon}\right)^{\frac{1}{4}}, \tag{I.4}$$

thus, η is commonly known as the *Kolmogorov scale*. Despite its heuristic deduction, equation I.4 has been widely corroborated experimentally (Sadd-oughi and Veeravalli, 1994) and accepted within the turbulence community.

[4] *Big whirls have little whirls that feed on their velocity, and little whirls have lesser whirls and so on to viscosity.* - L.F. Richardson

In order to characterize the energy cascade, it is convenient to translate the velocity field to its Fourier representation. At a first glance, the use of the Fourier transform may look like the compulsory need of using that tool for everything in physics, but there are several phenomenological reasons for doing so. As suggested by Batchelor (1953) and Davidson (2004), the recurring use of spectral analysis is coupled with the ability to easily discern different scales of motion. Moreover, the energy additivity of each component of motion is well represented by an orthogonal decomposition giving place subsequently to spectral energy decomposition. It also converts differential operators into multipliers and allows us to better define the degrees of freedom of a turbulent system (McComb, 1990).

Nevertheless, the use of such a powerful implement should always be handled with a couple of fair warnings. For instance, we need to keep in mind that turbulence consists primarily in the distribution of blovs, not a set of waves, which may lead to a phenomenological misconception, although some may suggest that it gives a relatively simpler picture of turbulence (McComb, 1990). Likewise, an infinite number of Fourier configurations may lead to the same energy spectrum, loosing some information regarding the real space turbulent pattern.

In the context of Fourier analysis, we shall first consider whether there may be a range of wavenumbers where the inertial transfer of energy is predominant. At this stage, we can assert that the smallest wavenumbers (biggest scales of motion due to the reciprocal relationship between wavenumber and spatial variables) are completely determined by the nature or source of turbulence; in this realm, the turbulent flow draws most of the energy from the mean flow. On the other hand, the largest wavenumbers should be determined by the translated Kolmogorov scale

$$k_d = \frac{1}{\eta} = \left(\frac{\epsilon}{\nu^3}\right)^{1/4}. \tag{I.5}$$

G.K. Batchelor (1953) has a great discussion regarding the independence of Fourier components for high wave numbers, giving arguments of how the presence of pressure forces tend to eliminate any directional preferences induced by large scale components of motion, giving rise to isotropic turbulence in the so called equilibrium range of wavenumbers. The reason for that name is because the statistical quantities in that range are independent of the large

scale components of turbulence and the forces are in approximate statistical equilibrium.

As summarized by Lesieur (2014), for stationary isotropic turbulence, the energy flux throughout different scales of motions is independent of the wavenumber k and equal to the viscous dissipation rate ϵ. Relying heavily on dimensional analysis, Kolmogorov's theory predicts that the energy spectrum for the inertial range should take the form

$$E(k) = K\epsilon^{2/3}k^{-5/3}, \tag{I.6}$$

where $K \approx 1.5$ is a universal constant. This result is usually associated or interpreted as a consequence of having a constant *spectral energy flux* through the inertial range.

There is another way to reach the same result, which will be helpful in the near future, by means of what it is generally called matched asymptotic analysis (Lundgren, 2003). In this approach, Kolmogorov's spectrum can be interpreted as an overlap between a large scale range, where the two relevant parameters are u and the integral scale L (the scale containing most of the kinetic energy), and a small scale range, where the the two critical parameters are ϵ and η. Taking $Re \gg 1$, both η and L become widely distanced and the overlap range only share as a common parameter ϵ[5], in this range using dimensional analysis we should return to the same expression in I.6.

I.2 Stratified Turbulence

For this work (as the title may already have hinted), it is within our main interest to study the effects of stratification on the development of turbulence. While the subject of stratification arises almost organically at the classification of the different layers composing the Earth's atmosphere, it is a rather prevalent consequence of having a fluid immersed in a strong and homogeneous gravitational field.

Heretofore we have discussed in some extent the aspects that characterize *statistically isotropic* turbulence, including what could be easily called the biggest achievement in understanding turbulence so far (in Kolmogorov's 1941

[5]Here we have used the well renowned Taylor (1935) hypothesis for the integral scale $L \sim u^3/\epsilon$.

theory). However, the isotropic condition arises from the fact that, in the absence of external forces, if we carry out a set of simulations or replicate the same experiment several times, the *average* behavior of a turbulent flow should not have any directional preferences[6], or as stated by Lesieur (2014) all the mean quantities concerning a finite set of spatial points are invariant under any simultaneous arbitrary rotation of the points with respect to the coordinate axes. In contrast, the case of stratified turbulence is a clear example where the presence of the gravitational field immediately imposes a favoured direction.

A stratified fluid can be broadly defined as a fluid with a background (or, average) density profile that decreases continuously with height. As a consequence of the density differences, any immersed fluid parcel would be subject to buoyancy forces and to related displacements. The simplest model for a continuously stratified fluid uses the Boussinesq approximation, which assumes that the density of a fluid varies only slightly, such that it can be considered constant except when it appears in a buoyancy related term, *i.e.* the density only appears when it is multiplied by the gravitational acceleration. In a nutshell, the Boussinesq approximation applies if the Mach number of the flow is small, propagation of sound or shock waves is not considered, the vertical scale of the flow is not too large, and the temperature differences in the fluid are small. Then the density can be treated as a constant in both the continuity and the momentum equations, except in the gravity term (Kundu and Cohen, 2002).

Considering the above, a reasonable attribute to further quantify (or measure) the amount of stratification is the buoyancy frequency N defined for the Boussinesq approximation by

$$N^2(z) \equiv -\frac{g}{\rho_0}\frac{\partial \bar{\rho}(z)}{\partial z}, \tag{I.7}$$

which is usually presented as the frequency at which a vertically and adiabatically displaced parcel will oscillate within a statically stable stratified fluid (Davidson, 2013). Here the density $\rho = \bar{\rho}(z) + \rho'$ is split into a background profile $\bar{\rho}(z)$, which is only a function of height, and a fluctuation ρ'; ρ_0 is the

[6]The importance of the statistical approach to turbulence is fundamental in this aspect, since in a single experiment (or simulation) any turbulent region is notoriously highly anisotropic.

reference density of the parcel and g is the gravitational acceleration, yet it may also be defined in terms of other scalars, like potential temperature.

In the real world, the presence of external forces is ubiquitous, but the significance of said forces vary according to each specific situation. Without a doubt, the impact of external forces is entirely dependent of the phenomenon's *scale*. Even though we are all immersed in the same gravitational field, the fall of an ant from the second floor of a building is not met with the same outcome as the respective fall from a human being because the dynamics of air resistance at the ant's scale is fundamentally different from that on the metre scale. At this point, it is natural to consider independently the effects on the dynamics of two characteristic length scales inside a stratified fluid: the vertical ($l_\uparrow$) and the horizontal ($l_\leftrightarrow$).

With the aim of constituting a solid framework where we would be able to discuss the consequences of stratification in turbulence, we need to impose certain restrictions by the means of dimensionless quantities; hence, we ask for the following requirements to be fulfilled as in Riley and Lindborg (2012):

- The ratio of the flow inertial forces with respect to buoyancy forces to be considerably small, which is outlined by the Froude number

$$F_\leftrightarrow = \frac{u}{N l_\leftrightarrow} \ll 1. \tag{I.8}$$

  This is a basic condition that imposes that stable stratification effects are the prevailing ones.

- Weak rotational effects, which implies a large Rossby number

$$Ro_\leftrightarrow = \frac{u}{f l_\leftrightarrow} \geq 1, \tag{I.9}$$

  where f is the local inertial frequency which accounts for the influence of Coriolis forces. On Earth's atmosphere, the range of scales where $Ro_\leftrightarrow \gg F_\leftrightarrow$ (i.e. $\frac{f}{N} \ll 1$) is usually denoted as the *mesoscale* ($\mathcal{O}(100)$km and smaller), here the effects of stratification are greater than the ones of rotation.

- Large *buoyancy* Reynolds number

$$Re_b \equiv F_\leftrightarrow^2 Re_\leftrightarrow = \frac{u^3}{\nu N^2 l_\leftrightarrow} \gg 1. \tag{I.10}$$

We have already discussed the essential role of large Reynolds numbers for the development of turbulence; nonetheless, it is important to notice that, as indicated by Brethouwer et al. (2007), for a fixed Re the stratification condition may suppress turbulence as $F_{\leftrightarrow}$ decreases, coming to the conclusion that strong stratification requires even larger Reynolds numbers. For that reason the fore quantity is able to recover the essence of high Reynolds numbers within the realm of stratified fluids.

Throughout this work we have tried to continuously emphasize the relevance of the experimental roots embedded in the study of turbulence. Nevertheless, we cannot ignore the notorious ascendancy of numerical simulations during the last decades and its current role in fluid dynamics. Due to the increased accessibility to greater computational power, numerical simulations have become one of the preferred tools to observe, qualify and quantify the myriad aspects related to turbulence, constituting another type of laboratory that allows us to easily modify parameters and visualize the consequences.

Taking into account the previous reflection, let us start presenting some of the experimental work that have shed light towards understanding the phenomenology of stratified turbulence. Lin and Pao (1979) in their review of wakes in stratified fluids recollected results of the stratified variation of classical turbulence experiments, like towing spheres or grid-flows. In the majority of the cases, turbulence grows in the usual chaotic manner, but after some time, the stratification appears to give place to some kind of regularity or organization to the vorticity structures (while keeping its stochastic nature). They concluded that vertical motions in a stratified fluid were generally inhibited, highlighting the emergence of quasi-two-dimensional structures. It is also worth mentioning the work exhibited by Billant and Chomaz (2000a), where they studied how a vertical columnar vortex present a new kind of *zig-zag instability* due to being immersed in a stratified fluid, noting the formation of horizontal structures as well.

These experimental observations coexist in agreement with a lot of their numerical simulation counterparts. For instance, Kimura and Herring (1996) found scattered "pancake-shaped" vortex patches lying in the horizontal plane suggesting them as a good candidate for the final structures in decaying stratified turbulence. The presence of these horizontal layers of blovs is shared across multiple references (e.g. Riley and deBruynKops (2003); Waite and Bartello

(2004); Brethouwer et al. (2007); Maffioli and Davidson (2016)) regardless of the different initial conditions or the use of forcing[7].

In summary, some of the distinguishing features found either experimentally or numerically about stratified turbulence is the decrease of the vertical scale ($l_\uparrow$) giving way to a predominance of horizontal layers of blovs. As a consequence of that, we would expect the primary velocity components to be horizontal, which are associated with a strong vertical component of vorticity (Davidson, 2004). Nevertheless, the intense shearing between layers leads to a strong horizontal component of vorticity as well, responsible for most of the energy dissipation. We need to remember that even though we are working with high Reynolds numbers, that does not necessarily imply a decorrelation between horizontal layers (Waite, 2014).

We have to acknowledge, based on both experiments and simulations, that there exists some transition where stratified turbulence gets organized in a quasi-two-dimensional manner. Nonetheless, if we continue to observe the evolution of blovs and recall the alleged *universality* of isotropic turbulence, it is natural to wonder if there exists a small enough scale of motion such that the turbulence would no longer be affected by the effects of stratification. Indeed, as marked by Lesieur (2014), if we take the hypothesis from Taylor (1935) for the energy dissipation rate ($\epsilon \sim u^3/l$) and search for a length scale l_O such that the associated Froude number is unitary (at this scale buoyancy no longer reigns as the main actor in the balance of forces), this yields what it is commonly known as the *Ozmidov* scale

$$l_O \equiv \left(\frac{\epsilon}{N^3}\right)^{1/2}. \tag{I.11}$$

According to Riley and Lindborg (2008) this scale can also be interpreted as well as the largest horizontal scale possessing sufficient kinetic energy to overturn. Notice that with the introduction of the Ozmidov scale, we can revisit our stratification conditions and see how the dimensionless quantities are translated in terms of l_O. For instance, the Froude number may be presented

[7] In general, the term *decaying turbulence* makes reference to setting initial conditions of the simulation and letting the system evolve and eventually die out due to dissipation; while *forced turbulence* makes allusion to the continuous injection of energy to the system in order to reach some kind of stationary state. Both cases are frequently used accordingly to the aspect of turbulence under study.

(with the help of the Taylor (1935) hypothesis) as

$$F = \left(\frac{l_O}{l}\right)^{2/3}, \tag{I.12}$$

which tells us that the effect of stratification on turbulence is imperceptible whenever $l \ll l_O$ and becomes dynamically important whenever the characteristic lengths of the blovs are greater than the Ozmidov scale (Ozmidov, 1965). Likewise, for the buoyancy Reynolds number, if we consider again Taylor's hypothesis, along with the definitions of the Kolmogorov and Ozmidov scales, we get that

$$Re_b \sim \left(\frac{l_O}{\eta}\right)^{3/4}, \tag{I.13}$$

therefore, a large Re_b immediately implies that there exists a vast range of separation between the scales l_O and η and, in this range, it is expected that the energy distribution should be the same as in I.6. As a final note, we need to acknowledge the fact that numerical simulations that fulfill at the same time the two conditions $Re_b \gg 1$ and $F_{\leftrightarrow} \ll 1$ are extremely demanding, mainly because of the need to be able to resolve Kolmogorov's scale, it can be shown that the total number of grid points ends up scaling as $Re_b^{9/4} F_{\leftrightarrow}^{-7/2}$ (Riley and Lindborg, 2012).

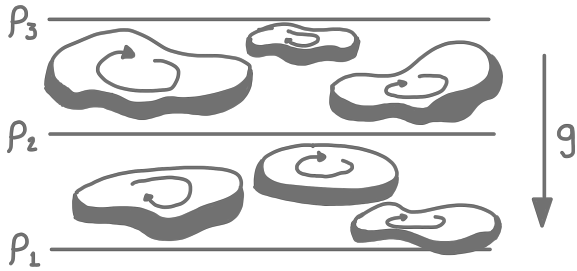

Figure I.2: Graphical representation of the horizontal structures or "pancake-blovs" in a stratified fluid.

Finally, there is still a legitimate question concerning the collapse of the vertical scale within the arrangement of turbulence into pancake-blovs (as they are schematically displayed in figure I.2): how is the ultimate size of $l_\uparrow$ settled or, to rephrase it in another way, how do the dimensionless parameters influence the vertical size of the blovs? In order to answer this question, it is rather useful and frequent to consider the equations of motion subject to the Boussinesq

approximation and follow the non-dimensionalization performed by Riley and Lelong (2000). In doing so it comes to light that even though strong stratification is defined by $F_{\leftrightarrow} \ll 1$, the magnitude of its vertical counterpart, $F_{\uparrow}$, restricts much of the behavior of turbulence. According to Billant and Chomaz (2001) the vertical Froude number tends to auto-adjust in order to have a balance between horizontal and vertical advection ($Fr_{\uparrow} \sim 1$), while conserving the anisotropy. Therefore, the vertical scale would be set by

$$l_{\uparrow} \sim \frac{u}{N}. \tag{I.14}$$

Consequently, several authors have named u/N the buoyancy scale (Waite, 2014).

I.2.1 Energy cascade in stratified turbulence

The next instinctive step, given our previous experience with isotropic turbulence regarding Kolmogorov's theory, is to discuss now the energy spectrum for the stratified case. An intuitive approach would be to exploit the distinctive anisotropy of the problem by introducing a decomposition that handles the vertical and horizontal components of the velocity field independently, preferably in their Fourier representation. Bearing that in mind, notice that when we translate the incompressibility condition ($\boldsymbol{\nabla} \cdot \mathbf{u} = 0$) to its Fourier counterpart, we find that

$$\mathbf{k} \cdot \hat{\mathbf{u}} = 0, \tag{I.15}$$

where $\hat{\mathbf{u}}$ is the Fourier transform of the velocity field, and $\mathbf{k} = (k_x, k_y, k_z)$ is the standard wave vector. Therefore, we can express the velocity field as a linear combination of two vectors orthogonal to the wave vector in what it is usually referred as the Craya-Herring representation (Kimura and Herring, 2012). For stratified turbulence, we can take advantage of the distinction of the vertical direction defining

$$\hat{\mathbf{e}}_v = \frac{\mathbf{k} \times \hat{\mathbf{z}}}{\|\mathbf{k} \times \hat{\mathbf{z}}\|} \quad \text{and} \quad \hat{\mathbf{e}}_w = \frac{\mathbf{k} \times \hat{\mathbf{e}}_v}{\|\mathbf{k} \times \hat{\mathbf{e}}_v\|}, \tag{I.16}$$

for all $\mathbf{k} \nparallel \hat{\mathbf{z}}$[8], in this way it can be shown that the inverse Fourier transform of $\phi_v \hat{\mathbf{e}}_v$ accounts exclusively for the horizontal and vortical behavior while the

[8] Flow with $\mathbf{k} \parallel \hat{\mathbf{z}}$ corresponds to vertically sheared, horizontally uniform horizontal flow, which is neither a wave nor a vortex (Smith and Waleffe, 2002)

one with $\phi_w \hat{\mathbf{e}}_w$ encompasses only the vertical and wavy nature of the velocity field (giving meaning to the original subscripts)(Lesieur, 2014).

It is important to mention at this point that the vortical component of the velocity field may satisfy, under certain conditions, a two-dimensional Navier–Stokes equation in the limit of *both* Froude numbers being small. This is one of the substantial premises by which Lilly (1983) proposed an inverse energy cascade (i.e. from small to large scales), as it is the case for two dimensional turbulence (Kraichnan, 1967). In that picture, stratified turbulence would be constituted by vertically decoupled two-dimensional layers; on the other hand, if we consider the scaling arguments of Billant and Chomaz (2001) the vertical collapse ends up setting $F_\uparrow \sim 1$, in that regard, we can no longer consider both Froude numbers to be negligible and Lilly's hypothesis does not keep standing. Likewise, the inverse cascade hypothesis has not received support from numerical simulations as indicated in Waite (2014).

Carrying on with the results from the Craya-Herring decomposition it is reasonable to consider independently the distribution of kinetic energy over the horizontal wave number components ($k_\leftrightarrow = \sqrt{k_x^2 + k_y^2}$) and the vertical component ($k_\uparrow = k_z$), besides the usual full kinetic energy spectrum $E(\|\mathbf{k}\|)$. Employing asymptotic analysis for the horizontal spectrum (Riley and Lindborg, 2012), at intermediate scales where viscous effects are weak, the only relevant parameters are ϵ and l_O, but when $F_\leftrightarrow \ll 1$ both the horizontal integral length and Ozmidov scale tend to become separated and the overlap region ends up characterized again only by ϵ, as it is the only shared parameter, resulting in a similar spectrum as for the isotropic turbulence

$$E(k_\leftrightarrow) = C_1 \epsilon^{2/3} k_\leftrightarrow^{-5/3}. \tag{I.17}$$

Analogously, for the vertical spectrum, the large scale range is defined mainly by u and N, while in the small scale range the main parameters are ϵ and N (Riley and Lindborg, 2012). As N is the only shared parameter, dimensional analysis yields the next result

$$E(k_\uparrow) = C_2 N^2 k_\uparrow^{-3}. \tag{I.18}$$

The same relation can be obtained by means of a *self-similarity* argument (Billant and Chomaz, 2001). If we believe that the vertical scale is determined by $l_\uparrow \sim u/N$ throughout *any* scale of motion then converting this condition

in Fourier space, we have that

$$\frac{1}{k_\uparrow} \sim \frac{\sqrt{k_\uparrow E(k_\uparrow)}}{N}, \tag{I.19}$$

which returns the same expression when we solve for the horizontal energy spectrum. Finally, we need to address the fact that the question of atmospheric mesoscale turbulence cascade its still widely open to this day and it is in the front row of the stratified turbulence problems.

I.3 Predictability

Now that we have settled the boundaries of the yard court where we would like to play (namely, stratified turbulence), it is necessary to come full circle and reprise the first attribute of turbulence that we have enlisted previously: its intrinsic chaotic nature. This characteristic, although some may argue beautiful in itself, seem to be troublesome to a species so deeply obsessed with trying to foretell on the basis of observation, experience, or scientific reason *what happens next?* Whether it is sports or weather, we have an innate tendency to search for predictability. Unfortunately, based on what we have discussed, we recognize that such a search may look fruitless when it comes to turbulence[9].

In our contemporary society, we have become accustomed to hold faithful weather forecasts that extend their accuracy to several days at the reach of our fingertips. At first glance, this poses an apparent contradiction: how is it possible to pull out predictability from such a chaotic system that houses a wide range of motions and is so sensitive to disturbances? With that question in mind, we will walk in a chronological fashion through some of the results and developments on the subject of turbulence predictability, in an attempt to give a complete background for the understanding of this work. It is necessary to acknowledge that the following reference trail aims to be, at best, representative of some of the work done within this field and any absent contribution is due to the lack of pages required to do them proper justice.

Even though weather forecasting has technically existed since the invention of the telegraph by allowing decent communication between observation sta-

[9] We have metaphorically sat the oracle itself at the desk and the only thing he has been able to do so far is to write the equations of motion and shrug to the ubiquitous presence of non linearity.

tions, the founder of modern weather forecasting is irrevocably L. F. Richardson in the early 20th century. At a time when the mere existence of computers eluded us from our most extroverted dreams, Richardson (1922) constructed a systematic numerical method for predicting the weather and showed its application by implementing a trial forecast, carrying each of the computations by hand![10] Albeit that forecast attempt was far from accurate, missing the calculation of pressure by a couple of orders of magnitude, his work gave way to the basic methodological structure for the Numerical Weather Prediction (NWP) used to this date.

Richardson's fruitless results are understandable (in fact, they are quite admirable, given the limitations) when we take into account that the *complete* weather forecasting problem is exorbitantly difficult due to the myriad of intricate factors involved (e.g. cloud dynamics, topographical forcing, etc). While the practical development of meteorology and NWP continued to grow on its own[11], driven mainly by the technological advances of the subsequent decades, it was pertinent to give a step aside and return to some unresolved theoretical questions of turbulence at large scales. In that way, the goal was to tackle a slightly different problem, filled with a plethora of idealizations but without forgetting the meteorological motivation of what these theoretical toy models can tell us about the characteristics of the planetary-scale motions.

Thompson (1957), concerned about the uncertainty of the atmosphere's future state could be restricted just by the economic incapacity of not having enough observation stations and the possible consequences of measuring errors, undertook a statistical study of the growth rate of small initial errors. He concluded that with the existing station network, small errors in observing the earth's atmosphere would tend to double in just a couple of days, but that the growth rate could be considerably reduced by increasing the density of observations. His results inspired some hope that accurate atmospheric predictions were reachable because unobserved errors at the small scales would not disrupt the large scale features.

More than a decade after, the forefather of chaos theory himself, E. N. Lorenz, published a seminal paper discussing the predictability of a flow which

[10] Presumably at the back of an ambulance in France while the Great War was unfolding (Lynch, 2006).

[11] This is a good time to emphasize that in this manuscript, our primary interest *is not* focused in the NWP predictability problem, but it is rather used as a starting point to our study.

possesses many scales of motion. In his work, Lorenz (1969) proposed to classify deterministic systems (systems with well established equations of motion) into different categories depending on how they statistically evolve with respect to errors imposed at the initial conditions. The main distinction between categories rest on whether at subsequent times the magnitude of the error between the "real or reference" and the "observed or predictor" system can always be tamed by making the initial error sufficiently small or whether it is inevitable that the discrepancy will become large, for any arbitrarily small initial error (i.e. unavoidable lost of predictability!). In the later case, for practical purposes, Lorenz (1969) argued that the behavior of the system is indistinguishable from that of an indeterministic one.

Taking inspiration from Thompson (1957), Lorenz (1969) dealt with ensembles of pairs of states (the real and the observed systems) of an isotropic and homogeneous two dimensional fluid; with the aid of simplifying assumptions, he proposes a statistical (quasinormal[12]) closure to develop a system of equations whose dependent variables are the ensemble average kinetic energies of the difference velocities at different scales, obtaining at the end solutions via numerical integration of these equations. The signature conclusion of Lorenz (1969), when analyzing several experiments, is that errors initially confined exclusively to the smallest scales of motion (i.e. the kinetic energy of the real and observed systems only differ at an specific range of high wavenumber vectors) may lead, by a continual process, to errors at the largest scales. This is what it is usually referred in the subsequent literature as an *inverse cascade* for the propagation of error and it basically says that errors at small scales tend to gradually contaminate the larger scale dynamics. This is then a deterministic system that posses an *intrinsic range of predictability*; that is, there is an inherent time interval within which errors surpass any prechosen magnitude. As shown in Experiment (C) from Lorenz (1969), in these kind of systems there is a point where cutting the initial error in half fails to boost the range of predictability in a significant way. In fact, Lorenz presented as a conclusion that the maximum range of meaningful predictability (the large scales are still not changed in a relevant way) for atmospheric models would be around 5-8 days.

[12] Throughout this section we will try to enunciate the specific type of statistical closure for that kind of reader filled with curiosity or well-versed within these techniques.

Lorenz's groundbreaking work gave birth to the classical school of turbulence predictability, where numerous researchers tried to expand his model or make a distinctive contribution within the subject (Leith, 1971; Lilly, 1972; Leith and Kraichnan, 1972; Herring et al., 1973). Most of these studies shared some similar results that can be gracefully summarized in the following points:

- Any scale k, belonging to the inertial range, is bound to be contaminated by error initially confined at high wavenumbers (we will use $k_E(t_0)$ to characterize the cutoff wavenumber at which the error is introduced in the initial conditions).
- The existence of an inverse cascade of error propagation from small to large scales is a direct consequence of the characteristic shape of the power law in the inertial range of the energy spectrum.
- The amount of predictability (whether a turbulent flow system falls in either of Lorenz's categories) described by the rate of error propagation has a direct association with the steepness of the slope of the inertial range.
- As both systems are, at the initial time, statistically correlated for all $k < k_E(t_0)$ in the inertial range, the decorrelation time due to the error propagation at k is, in some cases, independent of $k_E(t_0)$.
- The error-spectrum $E_\Delta(k,t)$, which is the spectrum of the kinetic energy of the difference of the velocities $\mathbf{u}^p - \mathbf{u}^r$ in systems p and r, grows with time in a *self-similar* fashion, where is the spatial average over the domain. This is a dimensional consequence of really being a function of $\{k, k_E, t\}$.

Lilly (1972) made special emphasis on the fact that whenever the energy spectrum presents a negative power law of the form $E(k) \sim k^{-n}$, on dimensional grounds, the timescale associated with the growth of the error (or loss of predictability at scale k) is

$$\tau(k) \sim k^{(n-3)/2}, \tag{I.20}$$

which may be considered proportional to the blov turnover time $(l/u(k))$. Among his conclusions, Lilly (1972) stated that the error amplitude tends to

grow exponentially while maintaining a shape preserving energy spectrum. Likewise, he concluded that the forcing mechanisms did not seem to make any relevant difference to the lost of predictability. Returning to the original concern of Thompson (1957),Lilly (1972) suggested that, as the growth of instabilities seems to be controlled by small scales, an increased resolution may still increase predictability.

Leith and Kraichnan (1972), while making use of a EDQNM[13] closure, compared the predictability between three and two dimensional isotropic turbulence with a stationary energy spectrum (i.e. with forcing). In their work, they determined that the predictability time could be extended as much as desired for 2D turbulence with -3 spectrum, while 3D turbulence with $-5/3$ still presented the same limited predictability time. On the phenomenological part of the error propagation, they argued that at the discontinuity between correlated and uncorrelated spectral regions, initially there is a downward sweeping out process to higher wavenumbers (due to the energy cascade), but then the error spectrum when it is fully developed moves toward lower wavenumbers at a rate consistent with scaling laws, blaming the upward inverse cascade to a *convective defasing mechanism*. For experiments with atmospheric parameters, they found that much of the knowledge remains beyond one week for large scale motions.

In the following decade, we can say that there was a transition period where the closure models began to coexist with the development of large eddy simulations (LES). Métais and Lesieur (1986) postulated that statistical closure theories, such as EDQNM, present an intrinsic problem on accurately representing the error spectrum, whenever nonlocal interactions between scales of very different sizes are not considered, or properly modeled. Likewise, Métais and Lesieur (1986), asserted in a comparative study that freely evolving three dimensional turbulence is more predictable than its stationary counterpart (up to 50% more predictable!); nonetheless, freely evolving turbulence still presented a similar contamination within large structures by an inverse cascade of error. Consequently, they argued that large *coherent structures* (such as the ones produced by barotropic instabilities, mixing layers or isolated vortices) immersed in turbulent flows present an experimentally extended predictabil-

[13] Which stands for Eddy Damped Quasi-Normal Markovian.

ity due to an increase with time of the large blov turnover time in the case of freely evolving turbulence.

Thereafter, Chollet and Métais (1989) carried large eddy simulations showing an agreement between their results and the ones obtained from EDQNM, in the same frame of homogeneous isotropic turbulence. This was a relevant result, because it pointed out that the inverse error cascade was not just a closure artifact. In this work, Chollet and Métais (1989) compared pairs of realizations of velocity fields departing from nearly the same initial conditions and assemble the most pertinent techniques to quantify error growth. From a phenomenological point of view, they interpreted the unpredictability growth as a combination of the shift in time, or space, of identified blovs and the shape, or size, evolution of blovs. Among their conclusions, they confirmed the backtransfer of error towards larger scales. However, they characterized the process of error spreading as mainly local (in terms of spectral space) and justified that interactions between similar scales are the first contributors to the existence of this phenomena, which may differ from 2D turbulence.

At this point, the classical picture of turbulence predictability seemed to be almost complete, with minor contributions added every now and then. Regardless, as the climate models continued to develop exponentially over time, Tribbia and Baumhefner (2004) considered pertinent to reexamine certain questions of the interscale influence in predictability error growth but in the framework of NWP. With their implementation of identical and imperfect twin experiments they found distinctive differences with the classical inverse cascade error growth and its mechanism. Its most important contribution is to be able to displace the everlasting attention from the inverse cascade process as the main participant to the loss of predictability. In their study, they concluded that errors grow preferentially at intermediate scales and that the primary role of the inverse cascade is to seed disturbances in the baroclinically active region of the spectrum. From there, errors tend to organize within synoptic[14] structures and amplify.

In contrast with the previous apparent rupture with the classical picture, Rotunno and Snyder (2008) went to the other extreme reprising the original statistical treatment developed in Lorenz's (almost to a mimeographical

[14] The synoptic scale is generally associated with a horizontal length scale of the order of 1000 kilometers or more. At this scale it is typical to find mid-latitude depressions such as cyclones.

but pedagogical extent), considering a surface quasigeostrophic (SQG) approach as a driving model instead of the plain two-dimensional vorticity equation (2DV) taken by Lorenz (1969). There are several advantages in doing so; mainly, SQG flow has the ability to replicate a "$-5/3$" spectrum seen at the mesoscale while sharing lots of the mathematical benevolences of 2DV. In other words, it is basically 2D turbulence but with 3D turbulence spectrum. In contrast, Lorenz's model has the physical inconsistency of using arbitrarily different spectra, when it has been experimentally and theoretically confirmed that the inertial range in 2D turbulence is only consistent with a "-3" spectrum (Kraichnan, 1967). In Rotunno and Snyder (2008), the error growth analysis reintroduced the critical importance of downscale error as a differetiator between $-5/3$ and -3 spectrum. In the former, downscale error spreading is much stronger than in the later, providing an explanation of how the continuous feedback generates a rapidly growing small-scale maximized error spectrum in 3D turbulence, while its absence allows the extension of predictability in the 2D case.

Shortly after, Morss et al. (2009) handed over a more realistic study regarding the link between the importance of the steepness of the spectral slope and the error growth dynamics, in isotropic homogeneous turbulence. Their motivation resides on the observations that the atmospheric kinetic energy has a transition from a -3 slope at synoptic scales to $-5/3$ at the mesoscale (Gage, 1985) and the capacity to address the problem with a model simpler than NWP models but able to encompass complex atmospheric flows: a multilevel quasigeostrophic model with high resolution. For their model, the error doubling time in the linear regime of error growth was approximately 1.2 days which was a substantial upgrade compared with doubling times on the order of minutes in Lorenz's model. They concluded that the main difference between the error behavior tied to a shallow slope (like a $-5/3$ regime) and a steeper one (like -3) is that the error spectra initially peaked at the smallest resolved scales for the former while it peaked at the energy containing scales for the later. In the first case, error saturation of small scales causes the peak in the error spectrum to shift towards larger scales.

At the same year, Ngan et al. (2009) highlighted the importance of revisiting the results of the classical picture with a modern approach. They preferred to use a Boussinesq model to study the predictability of rotating stratified tur-

bulence[15]. Ngan et al. (2009) analysed two limiting cases: subsynoptic scales where the effects of strong stratification are predominant and synoptic scales dominated by rotation with weak stratification. Doing twin simulations, they noticed that the evolution of the error spectra was significantly faster in the synoptic case. Furthermore, they did not find a self-similar decay in the subsynoptic flow, nor find a complete loss of predictability for this case. In resemblance with Tribbia and Baumhefner (2004), they postulated that beyond the Ozmidov scale, as we expect to have 3D isotropic turbulence, errors may serve as *seeds* for an inverse cascade to larger scales. One of their most important contributions was to emphizese how for anisotropic turbulence predictability may be strongly dependent of scale, subjugated to the value of the Rossby and Froude numbers. Likewise, they build a strong case to assert that predictability decay is mainly driven by turbulence but slowed by the presence of inertial waves. From their perspective, waves help to mitigate non-linear energy transfers and acknowledging the fact that as inertial waves dominate the dynamics of the larger scales, they provide an explanation for why such scales become more predictable.

Subsequently, Durran and Gingrich (2014) return their attention to what they believe was a fairly overlooked result from Lorenz (1969) himself: in experiment (B) Lorenz added the perturbations restricted to larger scales and showed that doing so it produces a comparable range of predictability to the experiment where errors were confined to small scales. With that in mind, Durran and Gingrich (2014) used a slightly modified version of the SQG model from Rotunno and Snyder (2008) to study the difference of adding error restricted to small scales and having a uniform relative error distribution throughout all scales. They stated that the loss of predictability by initial error with fixed amplitude was *independent* of their spatial scale when dealing with a $-5/3$ spectrum. Therefore, small relative errors at large scales could have a similar impact on the lost of predictability as large relative errors at small scales. Their results point to the fact that the mesoscale inherits its intrinsic predictability from the motion at large scales. Which leaves a satisfactory reply to *the possibility that weather forecasting may be limited by perturbations as trivial as the*

[15]The reader is strongly advised to at least skim over this particular reference due to its conspicuous closeness to the objectives and general framework of this thesis.

flapping of butterfly wings; in the end, said contributions should be dwarfed by errors in the larger scales.

Ngan et al. (2009) called for an implementation of modern statistical diagnostics (such as relative entropy or finite-size Lyapunov exponents), taken out from the interdisciplinary fields like information theory and complex systems analysis, to act as a much needed complement to the classical picture of turbulence predictability. Boffetta and Musacchio (2017), following a familiar scheme used in some of their previous work (Boffetta and Musacchio, 2001), responded to Ngan's call. In their work, Boffetta and Musacchio (2017) studied the predictability of isotropic homogeneous stationary turbulence on the basis of high resolution direct numerical simulation (DNS) at different Reynolds numbers by measuring the separation between near identical realizations and computing the leading Lyapunov exponent to indicate the rate of exponential growth of said separation. From their point of view, the strong chaoticity of turbulence does not spoil completely its predictability because of the ratio between the very fast time scales where perturbations originate and the time scale related for small perturbations to affect significantly the dynamics of the large scales; giving birth to a strange marriage between chaoticity and predictability time. In their results, they showed that the Lyapunov exponent has a dependency with the Reynolds number but with an unexpected scaling exponent, larger than the one suggested by dimensional analysis.

At the end of this reference carousel, we have the work of Yoshimatsu and Ariki (2019). They conducted a theoretical analysis based on a self-similarity assumption for the large-scale error field evolution, showing that the growth of the error energy spectrum is characterized by both the total error energy and the integral length scales of the error field. They corroborated their theoretical analysis with DNS simulations of 3D homogeneous isotropic turbulence. Their work is a modern retake to replicate some of the classical closure results. The amount of computational resources available nowadays allow us to use DNS to conduct our experiment with high definition simulations; that is one of the main reasons why we will continue with this approach in order to study the effects of stratification within the predictability framework.

I.4 Thesis objectives and format

As we can appreciate with the previous literature review, there is a broad predictability scheme and the areas of research are quite diverse within such a field. However, the main purposes of this manuscript can be summarized as follows:

- To unthread some of the general properties of stratified decaying turbulence numerical experiments and to examine them under various predictability diagnostics and to further extend the analysis behind the classical picture of isotropic turbulence predictability to this particular regime.

- To study the effects of the buoyancy Reynolds number on the predictability of stratified flows. First, by comparing the range of predictability by increasing Re_b. And then, comparing numerical experiments with different fluid parameters (such as stratification) but with similar Re_b.

- To unravel the global and local error dynamics on vertical and horizontal scales[16] and study their individual contributions on the predictability of the three-dimensional phenomenon as a whole.

- To examine the weight of the error introduction on the final outcome of the experiments by investigating the dependence of the results with respect to the geometry of the added perturbations in the numerical domain and the effects of initially restricting such perturbations to smaller scales.

After this chapter, the numerical scheme, simulation framework, and methodology are presented in chapter II. The dissection of the respective outcomes is exposed in chapter III. At the end, the corresponding conclusions with a summary of the results and the insight for future related works are shown in chapter IV.

[16] This alludes to the general growth of the error at different wavenumbers and the respective repercussions, as a whole, of the propagation of the error within the entire domain of the experiments.

Chapter II

Methodology

II.1 Equations of motion

Neglecting the effects of planetary rotation or any other external forces, the Boussinesq equations for a uniformly stratified fluid are:

$$\frac{\partial \mathbf{u}}{\partial t} + \mathbf{u} \cdot \nabla \mathbf{u} = -\frac{1}{\rho_0} \nabla p + b\hat{\mathbf{e}}_z + \nu \nabla^2 \mathbf{u}, \tag{II.1}$$

$$\frac{\partial b}{\partial t} + \mathbf{u} \cdot \nabla b + N^2 w = \kappa \nabla^2 b, \tag{II.2}$$

$$\nabla \cdot \mathbf{u} = 0, \tag{II.3}$$

where $\mathbf{u} = (u, v, w)$ is the velocity field, $\hat{\mathbf{e}}_z$ is the unitary vector in the vertical direction, p is the dynamic pressure, κ is the thermal diffusivity and we define the buoyancy as $b = -\frac{g}{\rho_0}\rho'$, where the density is decomposed as $\rho = \bar{\rho}(z) + \rho'$, with $|\rho'| \ll \bar{\rho}$ and ρ_0 is a constant reference density. We take the buoyancy frequency $N^2 = \frac{g}{\rho_0}\frac{\mathrm{d}\bar{\rho}}{\mathrm{d}z}$ to be constant. Many assumptions play an important role on the validity of such equations. For instance, the basis of this approximation is that we can encounter quite a few scenarios where the temperature and density do not present significant variations, yet the buoyancy force drives the motion. Hence, in the first equation, the density only affects the buoyancy term of the momentum equations and is taken constant for all the other terms (Kundu and Cohen, 2002). The second equation is the result of the usual thermodynamic diffusion equation for fluids. And the last one is the incompressibility condition, for which we usually require that the Mach

number (defined as u/c, where u is the characteristic flow speed and c is the speed of sound in the medium) be small enough, we neglect the propagation of sound or shock waves (those tend to carry unpleasent pressure variations) and we consider a sufficiently small vertical scale so that hydrostatic changes in pressure do not affect the density (Kundu and Cohen, 2002). At a first glance, all these conditions may seem too restrictive but keep into consideration that it is largely satisfied at small scales, and it's the simplest model for studying effects of continuous stratification on turbulence.

Analogously to the treatment of the Navier-Stokes equations we can present the momentum equation II.1 in terms of the vorticity:

$$\frac{\partial \boldsymbol{\omega}}{\partial t} = \boldsymbol{\nabla} \times (\mathbf{u} \times \boldsymbol{\omega}) + \alpha \begin{bmatrix} \partial T/\partial y \\ -\partial T/\partial x \\ 0 \end{bmatrix} + \nu \nabla^2 \boldsymbol{\omega}. \tag{II.4}$$

Notice that the term in square brackets is commonly associated with the baroclinic generation of vorticity. As a consequence, the vertical component of vorticity is not directly influenced by the buoyancy force.

II.2 Numerical model

The main advantage of equation II.4 is that if we are able to solve it (undoubtedly via a numerical method), we can always return to our original velocity variable by solving the associated Poisson equation:

$$\nabla^2 \mathbf{u} = -\boldsymbol{\nabla} \times \boldsymbol{\omega}. \tag{II.5}$$

At this point, we are presented with an ideal opportunity to resume our previous discussion on the importance of spectral decomposition as a vehicle to better understand turbulence, especially when we notice that elliptic equations such as II.5 are conveniently solved in its associated Fourier domain. Hence, for an arbitrary wave vector $\mathbf{k} = (k_x, k_y, k_z)$, equation II.5 takes the form:

$$-||\mathbf{k}||^2 \hat{\mathbf{u}} = i\mathbf{k} \times \hat{\boldsymbol{\omega}}, \tag{II.6}$$

where the hatted variables represent the Fourier counterpart of the original velocity and vorticity. We can readily see that the velocity is obtained by simply dividing the previous expression by the $||\mathbf{k}||^2$ factor. Now, in order to avoid

problems at the origin ($\mathbf{k} = 0$), we can consider *all* variables to be zero at the zero wave vector, which can be interpreted as the absence of a mean flow.

On this basis, our numerical model[1] presents the application of a spectral transform method with periodic boundary conditions on a cubic domain of size L^3 and an isotropic grid. To summarize, our goal is to integrate in time and in Fourier space equations II.2-II.4 (with an adequate time stepping scheme) while storing the model variables in physical space, using the Fast Fourier Transform (FFT) as the bridge to go back and forth. In this way, we can benefit from calculating certain quantities in the domain that is most convenient. For example, we can exploit the fact that quadratic nonlinearities are easiest to evaluate in the physical domain by simple point-wise multiplication. Whereas, differentiation is best computed in Fourier space, here we just need to multiplicate by a factor of "ik", with k being an arbitrary wavenumber.

Just as we have outlined the advantages within this approach, there are some downsides along the way. Dealing with pointwise multiplication, aliasing errors arise as they can be generated in attempting to evaluate the product of two poorly resolved waves on a numerical mesh (Durran, 2010). Furthermore, aliasing tends to incite numerical instabilities causing solutions to blow up. The immediate solution to this problem is to restrict the range of scales by truncating the amount of Fourier coefficients. We use the "two-thirds rule" which corresponds to truncate at $K_j = n_j/3$ (with $j \in \{x, y, z\}$ and n_j is the number of discrete wavenumbers in each direction) instead of using the *natural* choice of truncation wavenumbers $K_j = n_j/2$ given that this later option is not enough to counter all aliasing error (Durran, 2010).

Going back to the time stepping scheme, the equations are solved using a third order Adams Bashford method (AB3), with the viscous and diffusion terms treated with a Cranck-Nicolson approach. As discussed by Durran (2010), we only need to ensure the stability of the linear and advective terms (with a sufficiently small timestep) to also tame the numerical instabilities from the diffusion and viscous terms.

As a final remark, it is important to notice that, given the nature of our studied subject and the computational capabilities at the time, we are interested in resolving at every point of the grid the whole range of spatial and temporal

[1] We used the same spectral transform model that has been employed in several previous investigations of stratified turbulence (e.g. Waite (2011); Legaspi and Waite (2020)).

scales associated with turbulence, from the Kolmogorov scale, up to the integral scale. By this means, our numerical set up is commonly classified as a Direct Numerical Simulation (DNS) (Orszag, 1970), which in practice translates to having $\eta K_j \gtrsim 1$ for all $j \in \{x, y, z\}$.

II.3 Procedure

Following in the footsteps of several previous numerical studies of predictability (eg. Lilly (1972); Ngan et al. (2009)), our general objective is to characterize the *predictability error* that arises from the divergence between almost identical twin experiments that sprout from a common precursor run. Each of the parent runs presented in this work are initialized with isotropic random-phase velocity fields in close agreement to Maffioli and Davidson (2016)[2] which satisfies:

$$E(k) = \mu k^4 \exp\left(-k^2/k_p^2\right), \tag{II.7}$$

where $E(k) = \frac{1}{2}\langle \hat{\mathbf{u}}^* \cdot \hat{\mathbf{u}} \rangle$ is the three dimensional energy spectrum which is calculated averaging over spherical shells of radius k and μ is the amplitude of the initial spectrum. This amplitude is selected to ensure that the initial domain-averaged kinetic energy is normalized, meaning that the velocity scale is $\mathcal{O}(1)$. We also set $k_p = 5$, which sets the amplitude of the peak of the initial spectrum, located at $\sqrt{2}k_p$. The length scale of our experiments is characterized by this peak, in that way we have that $l = 2\pi/\sqrt{2}k_p$. Likewise, from the initial conditions we can estimate the characteristic flow speed using the normalization of kinetic energy and the isotropic set up as follows

$$E = \frac{1}{2}(u^2 + v^2 + w^2) = \frac{3}{2}u^2,$$

therefore $u = \sqrt{2/3}$ and the associated turn over time is $l/u \sim 1$. Notice that we make use of these initial conditions quantities in order to calculate the Froude and Reynolds numbers.

We let the parent simulation run until nearly reaching full development of turbulence, from 0 to 0.5 time units which is roughly half a turn over time,

[2] We take their initial condition set-up as the base of our simulations mainly because, as they briefly point out, they initialize both potential vorticity and internal gravity waves in stratified turbulence, without giving a particular preference to either of them.

and gather all the respective model variables. We take those outputs and use them as the initial conditions for the kickoff of the twins[3] simulations, running for an additional 5 time units with the same overall parameters as their parent simulation. Keep in mind that the runs are taken sufficiently long (in terms of the characteristic turn over time) that they are able to capture adequately the the development and then decay of turbulence). The key point in the twins' set up is that we introduce error to one of them (Artemis), while leaving the other one (Apollo) unperturbed, playing the role of the reference simulation. In this regard, the latter differs initially from the former on account of a small random perturbation introduced at all wavenumbers beyond a defined wavenumber cutoff.

	ν	N	Re	Re_b	F	k_O	k_d	$k_{\max}/k_d$
Jupiter (256)	2.0×10^{-3}	10	363	2.4	0.09	46	88	0.97
Zeus (512)	8.0×10^{-4}	10	907	4.6	0.09	52	163	1.04
Leto (1024)	3.1×10^{-4}	10	2285	12.1	0.09	51	331	1.03
Latona (2048)	1.2×10^{-4}	10	5758	35.5	0.09	47	688	0.99
Suez (512)	8.0×10^{-4}	6.5	907	11.4	0.14	27	166	1.03
Otel (1024)	3.1×10^{-4}	15	2285	4.1	0.06	107	309	1.10

Table II.1: Simulation parameters, non-dimensional numbers, and wavenumbers for all numerical experiments. The number next to the name of the numerical experiment alludes to its resolution (e.g. Jupiter (256) was set up with a resolution of 256^3).[4]

The first section of our experiments gravitates towards the inquiry of the significance of the Reynolds number and buoyancy Reynolds number for the predictability of stratified turbulence. To be concise, we conducted several experiments where we change, for different resolutions, the value of viscosity in accordance with resolving the Kolmogorov scale, while keeping the buoyancy frequency fixed, thus obtaining different values of Re_b. Consequently, we have changed the amplitude of the introduced error so we could have the same

[3] In order to avoid unimaginative reference calling, throughout this work we have named the twins *Apollo* and *Artemis*, while identifying the precursor simulation (used as the reference name for each numerical experiment) as different versions of their respective mythological parents (eg. *Zeus*, *Leto*).

[4] Notice that simulations with the same resolution share the same Reynolds number, which can work as a mnemonic trick at the moment of reading the results.

initial total error for all the experiments. In this way we can analyse the effects of having different Re and Re_b with same stratification. Next, we consider a set of experiments keeping the same viscosity and resolution as before but changing the buoyancy frequency. In this part we can study predictability of simulations with similar buoyancy Reynolds numbers resulting from different stratifications. In the final section, we explore in depth the effects of error introduction, since it is, by itself, a key factor over all the fore mentioned studies. Here, we emphasize on the implications of the geometry and range of error introduction. Taking our base experiment, Leto(1024), we carry out similar simulations, keeping the same general model parameters and just changing the wavenumber cutoff of error introduction (keeping the same initial total error energy), passing through the Ozmidov wavenumber as it characterizes two separate regions of the stratified turbulence spectrum. Likewise, we conduct an experiment where we add the error in a cylindrical portion of the domain instead of having it introduced by the domain complement of a sphere, making sure that the total amount of initial error keeps the same magnitude as in the base experiment. The advantage of studying so, in the frame of stratified turbulence, is to appraise if a cylindrical geometry would significantly change the results in the horizontal and vertical energy spectrum, as there is an initial contribution of error at every horizontal plane.

II.4 Diagnostics

In order to assess and quantify the amount of error propagation, we used a compilation of diagnostics presented across the numerical predictability literature (such as Leith and Kraichnan (1972); Chollet and Métais (1989); Ngan et al. (2009)). As we have advocated for the case that turbulence is better understood via a statistical and spectral analysis, an immediate first tool, having the velocity fields of each twin, is to calculate the (3D, horizontal and vertical) ensemble energy spectrum $E(k)$ at each timestep. Although this does not tell us much about predictability, we can compute in a similar manner the error energy spectrum $E_\Delta(k)$, which measures the wavenumber distribution of the decorrelation between the two fields. Given our periodic boundary conditions, we can define this quantity as the kinetic energy spectrum of the *difference* of

the velocity fields as follows

$$E_{\Delta}(k,t)\delta = \frac{1}{2}\sum_{\mathbf{k}'\in\mathcal{I}} |\underbrace{\hat{\mathbf{u}}_p(\mathbf{k},t)}_{Apollo} - \underbrace{\hat{\mathbf{u}}_r(\mathbf{k},t)}_{Artemis}|^2, \tag{II.8}$$

where

$$\mathcal{I} = \{\mathbf{k}'|k - \frac{\delta}{2} \leq k' < k + \frac{\delta}{2}\},$$

$\delta = 2\pi/L$, $\hat{\mathbf{u}}$ corresponds to the velocity in the Fourier domain and the subscripts p and r denote Apollo and Artemis, respectively. The next natural step would be to quantify the proportionality between the ensemble and error spectra. Thus, the ratio energy spectrum is defined by

$$R(k,t) = \frac{E_{\Delta}(k,t)}{E(k,t)}. \tag{II.9}$$

It is important to recall that Leith and Kraichnan (1972) showed that in both isotropic 2D and 3D turbulence this ratio spectrum develops and moves towards lower wavenumbers in a "self-similar" form (*i.e.* it retains its shape and scaling properties as it evolves in time). Notice that for an arbitrary wave vector $\mathbf{k}_0$, we can express the error kinetic energy as

$$2\cdot\underbrace{\frac{1}{2}\left(\frac{|\hat{\mathbf{u}}_p(\mathbf{k}_0,t)|^2}{2} + \frac{|\hat{\mathbf{u}}_r(\mathbf{k}_0,t)|^2}{2}\right)}_{\text{Ensemble KE}} - \underbrace{\mathrm{Re}\{\hat{\mathbf{u}}_p(\mathbf{k}_0,t)\cdot\hat{\mathbf{u}}_r^*(\mathbf{k}_0,t)\}}_{\text{Correlation}}, \tag{II.10}$$

where the ensemble KE refers to the average of the kinetic energy of each of the twins. Therefore as the fields reach full decorrelation at a given scale, the preceding function reaches its maximum value at $R(k,t) = 2$, in that case we will consider that the error has hit full saturation.

As it is rather challenging to interpret all the implications and subtleties by looking just at spectra, it is convenient to incorporate a handful of time series analysis that would let us understand the overall error evolution. For instance, the total error kinetic energy with respect to time is expressed by

$$e(t) = \sum_k E_{\Delta}(k,t), \tag{II.11}$$

which describes the total amount of dissimilitude between velocity fields. Now, the associated time series of II.9 would be given by

$$\sigma(t) = \frac{\sum_k E_{\Delta}(k,t)}{\sum_k E(k,t)}. \tag{II.12}$$

Both of these temporal development representations are great summaries of the *global* error propagation. However, for practical purposes, they tell a somewhat similar story. Let's not lose sight of the fact that our main interest lies in the *local* error dynamics since the existence of an inverse error cascade is usually attributed to the interaction between neighboring scales (chapter I). For that reason, we have replaced $\sigma(t)$ from our repertoire of tools, and instead incorporated the time series of the error ratio at a given scale of interest, namely: $r_K(t) = R(K, t)$.

The last implemented diagnostic is also heavily inspired by the error inverse cascade. Under the premise of a progressive phenomenon, given the insertion of error at small scales, we would be interested in characterizing the wavenumber from which the error has contaminated all the subsequent scales at any given time. This is commonly referred as the error wavenumber or error wavefront (Chollet and Métais, 1989; Ngan et al., 2009) and is defined by the wavenumber at which the ratio spectra reaches a pre-established threshold:

$$\kappa_e(t) : R(\kappa_e, t) = \gamma, \tag{II.13}$$

with $\gamma \in (0, 1)$. One immediate advantage is that κ_e describes the time evolution of error locally.

Even though several studies take $\gamma = \frac{1}{2}$ (inspired by Lorenz's original interest in the doubling error time), Chollet and Métais (1989) argue that this quantity should be small enough in order to place the wavenumber κ_e both in the correct range of error spectrum (k^4 for isotropic decaying turbulence) and in the rage of explicitly computed wave numbers. Following Chollet and Métais (1989), we have taken $\gamma = 0.01$ for all the experiments as well. Note that $\kappa_e(t)$ is expected to be a monotonically decreasing function as the front propagates to larger scales and previous studies have obtained a respective power-law scaling for this quantity (Leith and Kraichnan, 1972; Chollet and Métais, 1989).

Chapter III

Results

III.1 Leto (1024)$_{\mathcal{P}}$, in depth

In an attempt to better understand the overall study of the various conducted experiments and the contrast between them, it is important to first devote the beginning of this chapter to a complete dissection of just one experiment: Leto (1024)$_{\mathcal{P}}$. In that way, the reader has an opportunity to become better familiarized with stratified turbulence simulations and the interpretation of the following results.

Even though most of our results heavily rely on spectral analysis, we cannot forget the visual nature of turbulence and its significance in understanding the evolution of the underlying phenomena. With that in mind, we begin by presenting a proper visualization of the velocity and vorticity fields in figures III.1 and III.2. Without a doubt, the velocity fields are a great launching analysis pad since regardless of our background, it is one of the quantities with which we are certainly most familiar. At the first row of figure III.1 we can basically observe the general initial evolution of all our numerical experiments. The isotropic random-phase velocity fields have just barely developed and, as a result, we encounter a similar picture across the different planes at $t = 0.5$. In other words, at the time of the conception of the twins, the turbulence has not significantly lost its isotropic nature inherited from the initial conditions. At the subsequent times ($t = 2.9$ and $t = 5.30$), the full display of anisotropy is observed, as the vertical slices (in the last two columns) show how the turbu-

lence unfolds and organizes in horizontal layers. The horizontal slice (in the first column) doesn't present any particular type of directional preference in its development. One important thing to notice is that each of the panels has its own colorbar. As time goes by, the overall velocity magnitudes decrease as expected when dealing with decaying turbulence. If we kept the initial colorbar, the second and third row would no longer look so dramatic and would have lighter colors instead. Now, as previously discussed in chapter I, the vor-

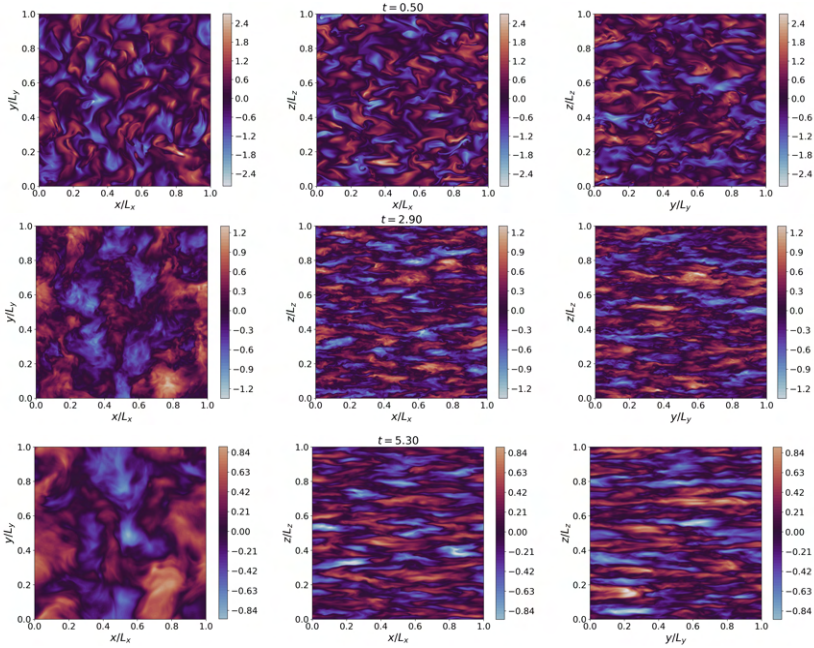

Figure III.1: Two-dimensional slices showing the y-component of the velocity at different planes in the middle of the domain of Leto (1024) . From left to right, the Π_{XY}, Π_{XZ}, Π_{YZ} planes are respectively displayed, marking their temporal development with each row (from top to bottom: $t = 0.5, 2.9, 5.3$).

ticity is a prime quantity to unravel and discern the nature of turbulence. In figure III.2, we compare the time progression of the y-component of vorticity in the Π_{XY}, Π_{YZ} planes. At the initial times ($t = 0.5$), we get the same kind of outcome as in the velocity field analysis. However, there is no noticeable directional preference in any of the two panels. At $t = 2.9$ we can contemplate the mixing nature of turbulence. On the right panel, layers of strong shear

are clearly visible, especially at later times, along with disturbances resembling shear instabilities. Lastly, on the third row, we can identify that the stratification has organized those instabilities in wider horizontal layers on the right panel, which is a direct reference to the famous pancake blovs addressed earlier.

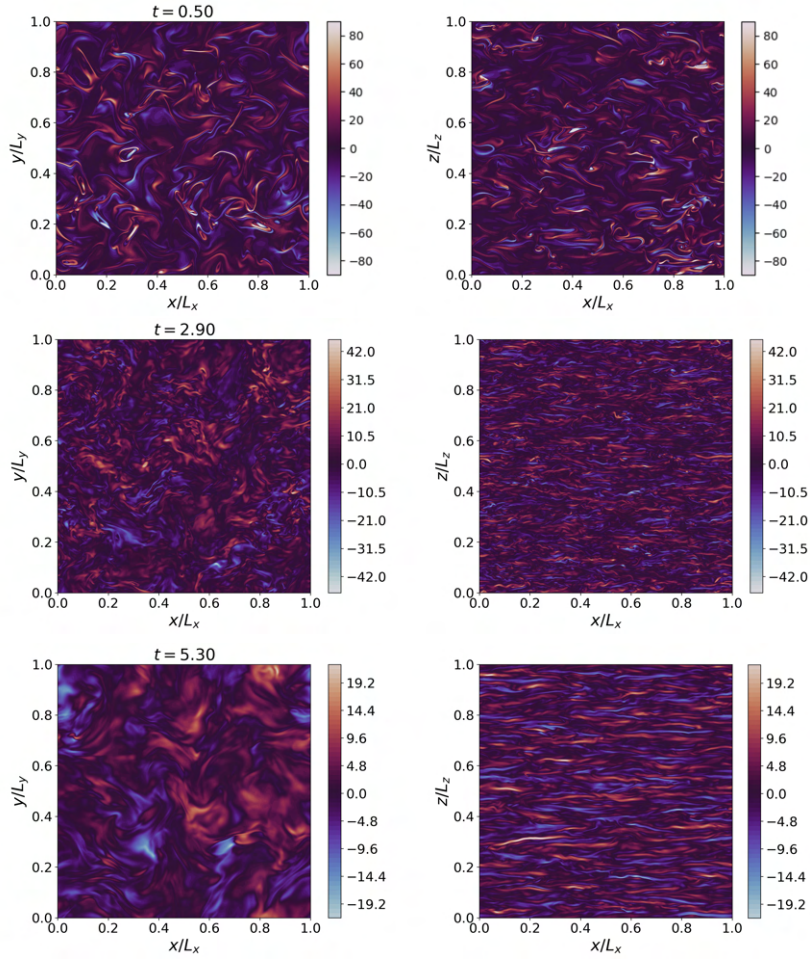

Figure III.2: Slices of the y-component of vorticity taken at the middle of the domain of Leto (1024) . From left to right column, the Π_{XY}, Π_{XZ} planes are respectively displayed, with their temporal development at the same times as in figure III.1.

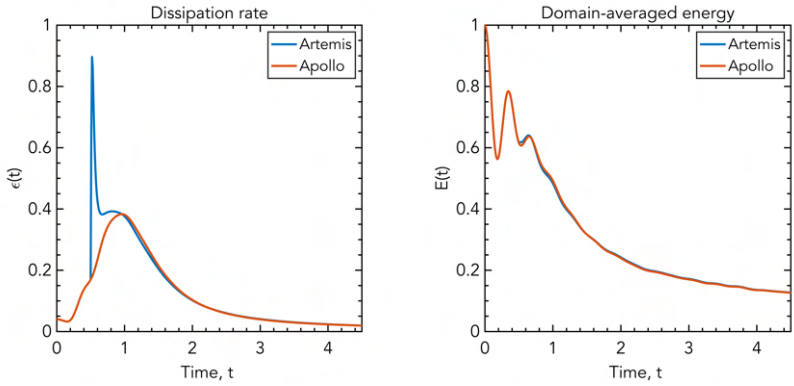

Figure III.3: Time series of domain averaged kinetic energy dissipation rate and kinetic energy of each twin simulation for Leto (1024) .

Next, we discuss the time series of two important quantities that characterize turbulence. In the left panel of figure III.3 we have the dissipation rate of both twins. As expected, the time series are identical for $t \in [0, 0.5]$ (as this part represent the parent run), but once the error is introduced we can see a significant jump for the perturbed twin Artemis. This shouldn't be surprising, as we have abruptly changed the small scales by introducing the error, some of the noise is dissipated, leading to a short increase in dissipation in the perturbed twin. After that jump, we can distinguish that both graphs share a similar path, this is well explained by Taylor's hypothesis (Taylor, 1935) because one of its consequences is that the dissipation is subject mainly to large scales that do not directly perceive the effects of viscosity after a turn over time.

In other words, the dissipation rate of Artemis returns to the expected value as determined by the unperturbed large scales. If we go to the right panel of III.3, we can appreciate the hierarchy of the large scales as well. There we can see that in spite of altering the domain averaged energy while adding the perturbations, as they are introduced over the small scales, they do not represent a significant change as the mean energy is largely contained in by the large scales. So far, we have outlined general aspects of stratified turbulence simulations, such as field visualization, kinetic energy and dissipation. Now, we are going to explore some of the predictability diagnostics, starting with the ensemble kinetic energy spectra. If we concentrate our attention on the first couple of outputs at times $t = 0.5$ and $t = 1$, we can observe that in figure III.4 the ini-

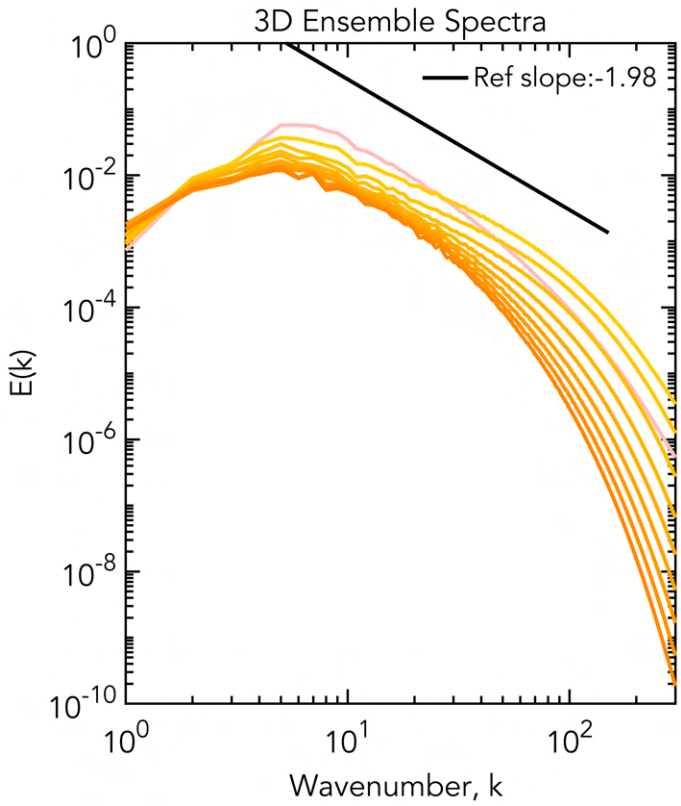

Figure III.4: 3D ensemble kinetic energy spectra of Leto (1024) , the time progression is given by the color gradient at each spectral line, from lighter to darker tones. The spectra are plotted each 0.5 time units from 0.5 to 5.5, highlighting the spectrum at t=0.5 with a different color. The reference slope is calculated at the time of maximum dissipation for the unperturbed twin (which roughly coincides with one turnover time).

tial spectrum is steep and then, as the dissipation increases, the spectrum gets shallower, which is characteristic of decaying turbulence. We can also notice that the spectra are equally spaced at the beginning and then they start to get closer, for large wavenumbers. As these figures are set in a logarithmic scale, given the spacing between lines, we may infer an exponential decay in early times.

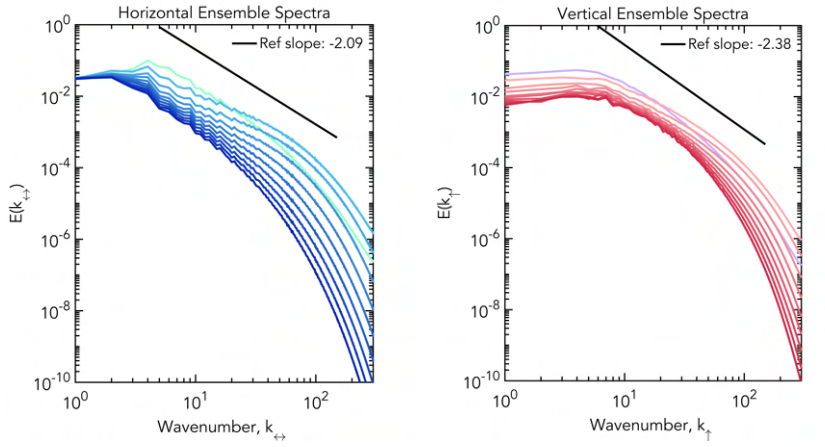

Figure III.5: Horizontal and vertical ensemble spectra of Leto (1024) , each line represent the kinetic energy spectrum at a different time and the time progression is given by the associated color gradient, from light to dark. The spectra are plotted each 0.5 time units from 0.5 to 5.5, highlighting the spectrum at t=0.5 with a different color. The reference slope is calculated at the time of maximum dissipation for the unperturbed twin (which roughly coincides with one turnover time).

Moving on to the horizontal and vertical counterparts of the ensemble spectra, there is a clear distinction with respect to the general shape and slopes. For instance, the horizontal spectra resembles in both aspects the 3D spectra, having that concentration of spectra at large scales (there is less decay at the smallest wavenumbers and more distance between spectra as $k_{\leftrightarrow}$ gets larger) and a somewhat similar slope. On the other hand the distinctive shape of the vertical spectra, helps us to understand the anisotropy of this type of turbulence as well, here the spacing between lines is similar across all vertical wavenumbers at early times.

As discussed in chapter II, we can begin exploring the real consequences of the addition of perturbations regarding predictability by referring to the error spectra. Spectra of error KE are shown in figure III.6. We can observe how the initial error is introduced by looking at the lightest spectra located at the bottom-right of figure III.6. Keeping in mind that the error is introduced at $k \geq 20$, then the initial spectrum has naturally the shape of a step function.

Moreover, the error grows hastily over all possible wavenumbers in a rather explosive fashion. Right away, the error grows very high at large k, but it's relatively low for small wavenumbers. We can also see that the spectra develops in a "self-similar" fashion, which alludes to the fact that it retains the same shape as the error propagates towards larger scales. As discussed by Ngan et al. (2009), the self-similar nature of the turbulence cascade of energy most likely yields the self-similar behavior of the error spectra.

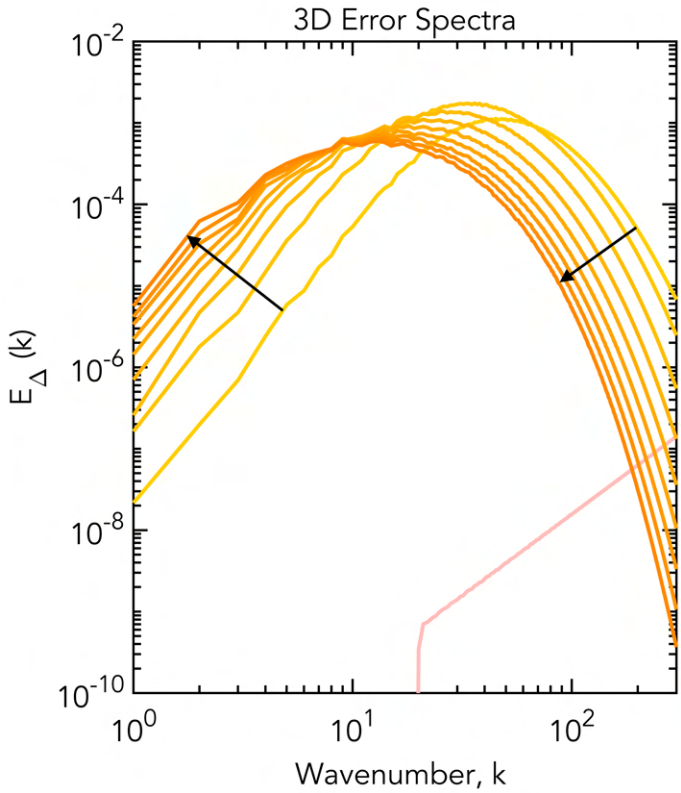

Figure III.6: 3D error kinetic energy spectra of Leto (1024), the auxiliary arrows are added to make emphasis on the time evolution direction of the spectra. The spectra are plotted each 0.5 time units from 0.5 to 5.5, highlighting the spectrum at t=0.5 with a different color.

Following the time evolution of the spectra, we can appreciate the emergence of two distinctive regions due to their contrasting behavior. As it is highlighted by the arrows in III.6: at large scales the error grows progressively

(characterizing the famous inverse error cascade!), while at small scales, the error saturates quickly and then decreases (mainly because of the decaying nature of our experiment). Even though it is difficult to assign a clear separation between those regions, notice that there is an intermediate range of scales, around $k \sim 10$, where both components balance out. This intermediate scale may be a function of the buoyancy Reynolds number and its meaning could become relevant for further research.

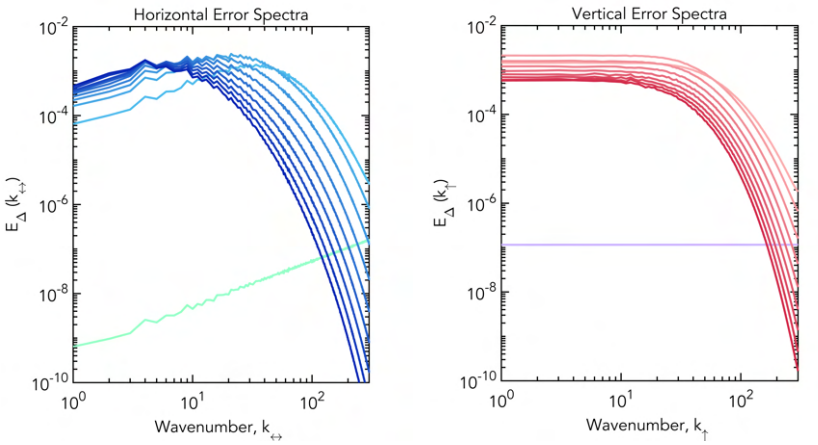

Figure III.7: Horizontal and vertical error spectra for Leto (1024) . The spectra are plotted each 0.5 time units from 0.5 to 5.5, highlighting the spectrum at t=0.5 with a different color.

An interesting story unfolds when we decompose the error spectra in its horizontal and vertical wavenumber components as shown in figure III.7. Starting with the shape of the initial error spectrum, we have a line with positive slope for the horizontal wavenumbers, while it is a constant for all the vertical wavenumbers. This is a direct consequence of the geometry involved with the error introduction. Remember that we have introduced random noise with a constant amplitude for all wave vectors such that $k \geq 20$ (*i.e.* filling the cube in Fourier space with error outside the sphere of radius 20). In that way, if we sweep through vertical wavenumbers, we would find the same amount of error in each plane with exception of those planes that pass through the empty sphere; however, the cross-section of the sphere space is negligible with respect to the total amount of wavenumbers, the result is an almost constant distribu-

tion for the initial error spectrum. Analogously, as we go to larger $k_{\leftrightarrow}$ (now with cylinders) the amount of error grows proportionally to the radius, having as a result a linear initial horizontal spectrum. After the initial error introduction, we have two completely different stories. For the horizontal spectra, there is a similar inverse cascade of error using the same arguments as in the isotropic case. Whereas for the vertical spectra, the error grows uniformly and instantaneously to *all* possible vertical scales, and then it relaxes uniformly as well. here is no visible inverse cascade of error for this case.

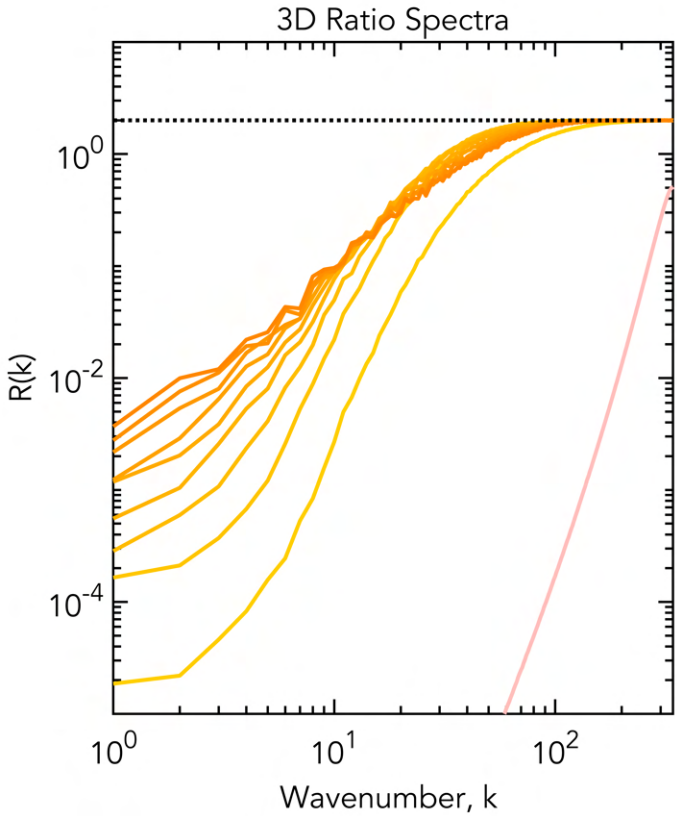

Figure III.8: 3D error ratio spectra of Leto (1024) . The dotted reference line is a constant at $R(k) = 2$, which denotes the saturation value of the error ratio. The spectra are plotted each 0.5 time units from 0.5 to 5.5, highlighting the spectrum at t=0.5 with a different color.

Lastly, we have the error ratio spectra presented in figures III.8 and III.9. These figures complete the picture of predictability on stratified turbulence due to their discernible and fathomable nature. Starting with the 3D case (III.8), the error propagation towards larger scales is evident, as the spectra move to smaller wavenumbers. In fact, we can appreciate that the error saturates rather quickly for $k \gtrsim 70$, which means that for small scales there is a (almost instantaneous) complete loss of predictability as both twin fields present total decorrelation between each other. If we were dealing with forced turbulence instead, it is likely that the error would have had the opportunity to contaminate and saturate even larger scales.

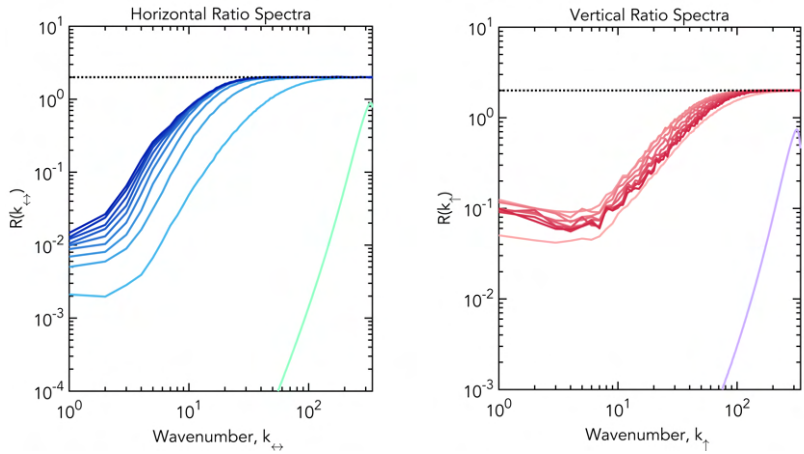

Figure III.9: Horizontal and vertical error ratio spectra for Leto(1024). The dotted line is the reference constant, which denotes the error saturation value. The spectra are plotted each 0.5 time units from 0.5 to 5.5, highlighting the spectrum at t=0.5 with a different color.

The horizontal and vertical decomposition of error ratio spectra neatly corroborates the assertion of an inverse error cascade for the horizontal case, and the lack of it for the vertical case. That is due to the fact that in the left panel of figure III.9, we can notice the same type of self-similar and continuous growth of error towards smaller horizontal wavenumbers, while in the right panel the relative error grows just in the first couple of outputs, then it stabilizes and remains practically the same for the subsequent times.

For the vertical case, the error dynamics are mostly driven by the decaying nature of turbulence instead. Even though the error dynamics are different, we still observe error saturation for the small scales in both cases. Indeed, for the horizontal ratio spectra the range of saturated wavenumbers is even wider than in the three-dimensional case, beyond $k_{\leftrightarrow} \sim 30$ there is full saturation of error; whereas in the vertical ratio spectra, the saturation interval starts around $k_{\uparrow} \sim 80$. These results are consistent with our stratified turbulence cartoon of pancake blovs. If we think on the imposed layer organization of turbulence due to the presence of the gravitational field, we would have expected the vertical component to be more predictable, as the velocity fields are somewhat restricted to freely evolve and reach higher values in the vertical direction. On the other hand, the horizontal components of the velocity field enjoy more sovereignty and, as a result, its error dynamics tend to be closer to the classical isotropic inverse cascade frame. We can argue that the overall amount of predictability in the three-dimensional case is therefore the addition of the predictability contributions from the vertical and horizontal components, and the balance between them.

III.2 Predictability dependency on buoyancy Reynolds number

Now that we are familiarized with the schematic methodology and analysis, the next step is to present the main results of our study of predictability within stratified turbulence. First, we exhibit four experiments with the same stratification, keeping the buoyancy frequency at $N = 10$, while decreasing the viscosity (and therefore increasing the resolution) in order to gradually increase Re and Re_b as displayed in table II.1. After discussing the associated results, the next section gives a comparison between experiments with similar Re_b obtained with different stratification and viscosity. In that way, we can objectively quantify the weight that the buoyancy Reynolds number has with respect to the amount of predictability obtainable.

III.2.1 Different Re_b with same stratification

Following the footprint traced in section III.1, we start by looking at the ensemble energy spectra in figure III.10. Here, we can see that as the buoyancy Reynolds number increases, from Jupiter (256) with $Re_b = 2.4$ to Latona (2048) with $Re_b = 35.5$, the slope of the ensemble spectra gets shallower as well. Otherwise, there is a similar behavior across the panels.

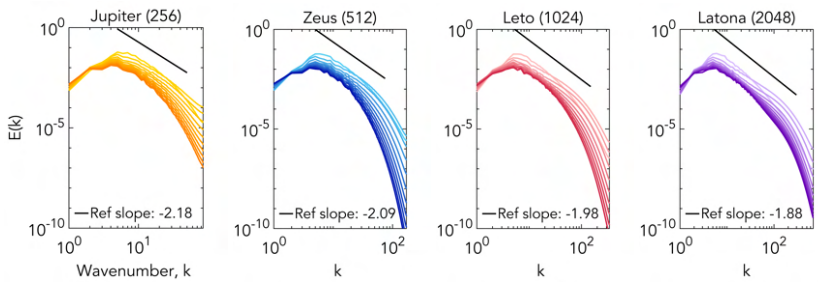

Figure III.10: Ensemble kinetic energy spectra of Jupiter (256) , Zeus (512) , Leto (1024) and Latona (2048) . The time progression is given by the color gradient at each spectral line, from lighter to darker tones. The spectra are plotted each 0.5 time units from 0.5 to 5.5. The reference slope is calculated at the time of maximum dissipation for the unperturbed twin (which roughly coincides with one turnover time) from $k = 5$ to $k = k_d$.

Next, we have the horizontal and vertical ensemble spectra in figures III.11 and III.12[1]. Notice that the reference slopes for the horizontal spectra of the experiments with high Re_b tend to a value in close agreement with the Lindborg (2006) and Brethouwer et al. (2007) theoretical $-5/3$ slope for strongly stratified turbulence. In fact, we can appreciate how this power law region becomes better defined as the experiments present more stratification, with Latona (2048) being the most recognizable case. However, we are unable to corroborate the -3 slope for the vertical wavenumber distribution, this is consistent to other studies like Maffioli and Davidson (2016).

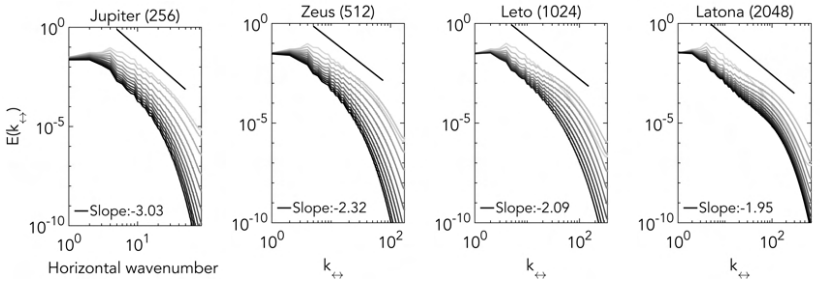

Figure III.11: Horizontal kinetic energy spectra ensemble of Jupiter (256) , Zeus (512) , Leto (1024) and Latona (2048) . The reference slope is calculated at the time of maximum dissipation for the unperturbed twin (which roughly coincides with one turnover time).

Regarding the predictability insight that these experiments can offer us, we would beforehand expect all of them to exhibit an inevitable loss of predictability. That is because they would fall into the *third* predictability category of Lorenz (1969), which states that the error of flows with spectrum slope shallower than -3 cannot be reduced no matter how small the initial error is taken. At first sight, this premise could be further extended to the horizontal and vertical ensemble spectra. However, there is a clear distinction between the behavior of these last two. Keep in mind that numerous studies indicate the existence of an energy cascade for the horizontal spectrum (Lindborg, 2006; Brethouwer et al., 2007), whereas it is not the same case for the vertical scales. Therefore, even though the vertical spectra present a shallow slope (compared

[1]Throughout this entire section, the vertical and horizontal spectra will be depicted in grayscale to to distinguish them from the isotropic wavenumber spectra.

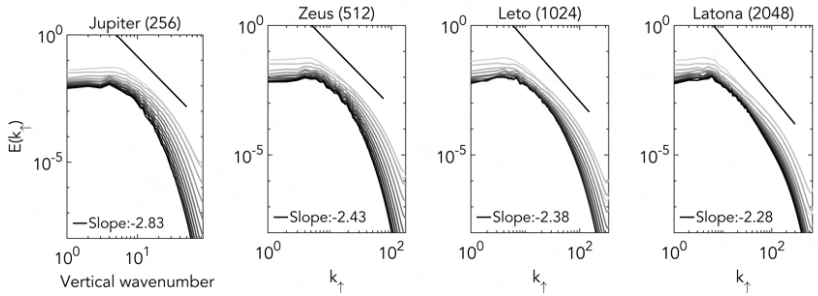

Figure III.12: Vertical kinetic energy spectra ensemble of Jupiter (256) , Zeus (512) , Leto (1024) and Latona (2048) . The reference slope is calculated at the time of maximum dissipation for the unperturbed twin (which roughly coincides with one turnover time).

to -3), this does not automatically implies the existence of an inverse cascade of error as set out in Lorenz's framework.

Next, we present the error (or difference) spectra in figure III.13 with its horizontal and vertical counterparts in figures III.14 and III.15, respectively. We identify the same shape preserving evolution as previously discussed in section III.1. All of them present two distinguishing regions: one characterized by the decaying nature where the error spectra progressively decrease and the other characterized by the contamination of error towards larger scales. The scale at which these two regions reach some kind of balance, moves *modestly* towards larger wavenumbers as we change from experiment with higher buoyancy Reynolds numbers, from $k \sim 7$ in Jupiter (256) to $k \sim 12$ in Latona (2048) . This is certainly intriguing given that the range of wavenumbers increases significantly at each subsequent experiment (consequence of increasing the resolution while decreasing the viscosity to obtain higher Re_b).

Furthermore, we can appreciate that the spectra get closer to each other as Re_b increases, particularly at the decaying region. Sharing a similar line of thought with Morss et al. (2009), in flows with shallow spectral slope, small scales initially experience a faster error growth rate until the perturbations grow large enough that small-scale errors begin to saturate (*i.e.* the velocity fields present total statistical decorrelation at those scales). After that, the large scales start to take over the perturbation growth dynamics and, as a consequence, the error growth rate slows down.

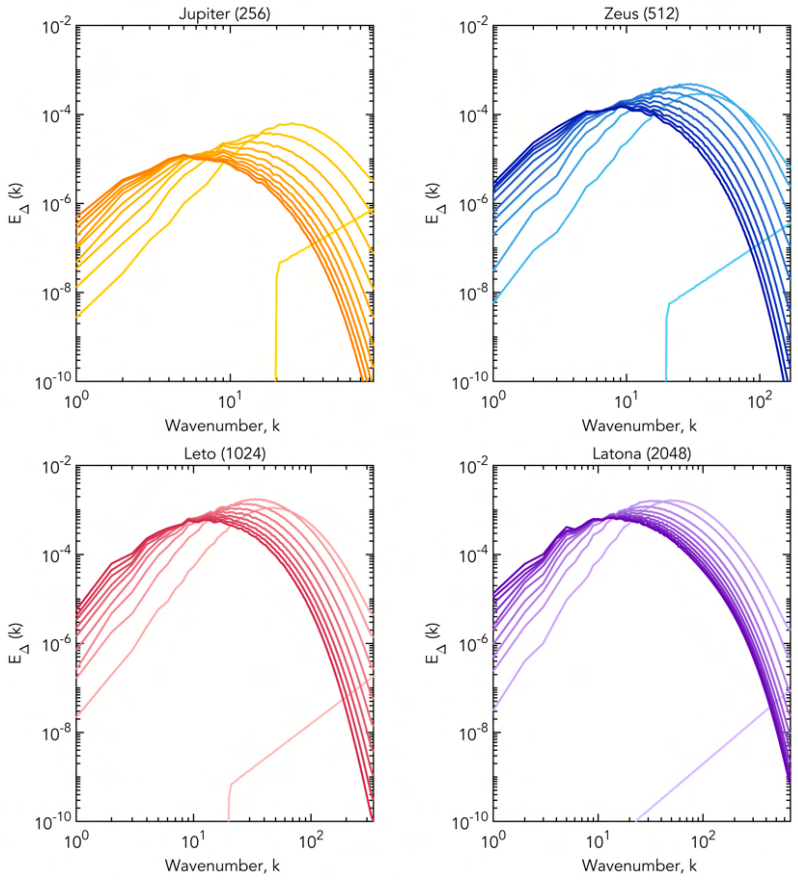

Figure III.13: Error kinetic energy spectra of Jupiter (256) , Zeus (512) , Leto (1024) and Latona (2048) . The spectra are plotted each 0.5 time units from 0.5 to 5.5.

Moving on to the horizontal and vertical error spectra decomposition, the presented outcome clearly corroborates the existence of an inverse cascade of error for the horizontal error spectra in figure III.14. There is a strong propagation of error from the first spectral line to the second in all the iterations. The strength of the inverse cascade of error can be examined by looking at the amplitude of the final spectral distribution and compare it with the initial spectrum (without forgetting that we are dealing with decaying turbulence). Comparing the furthest cases, Jupiter (256) and Latona (2048) , the global

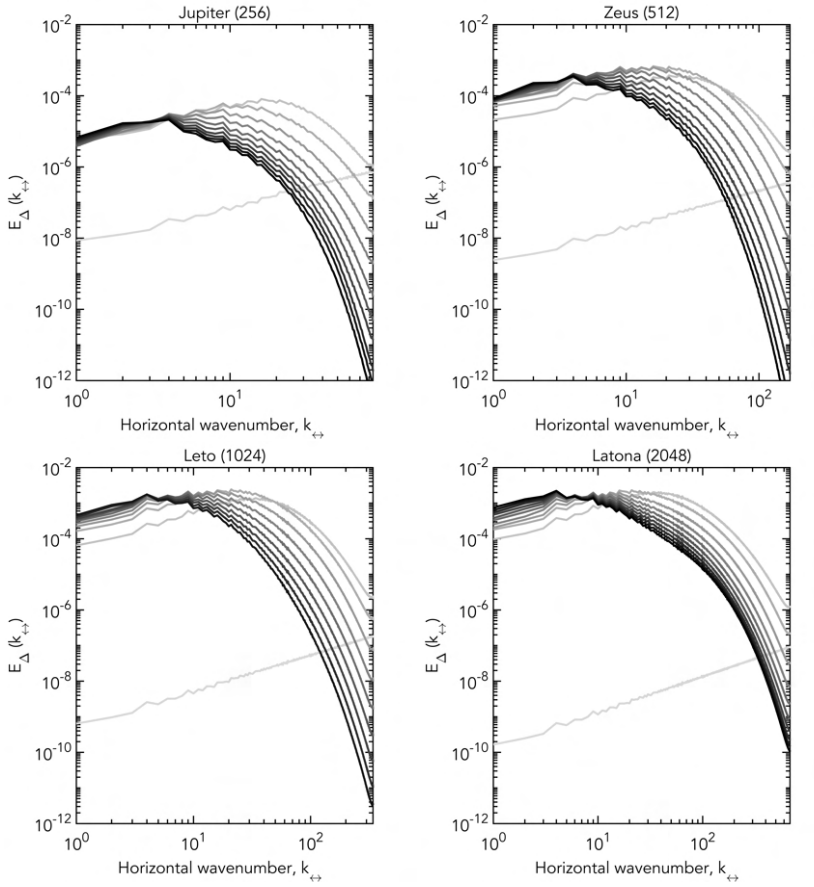

Figure III.14: Horizontal error kinetic energy spectra of Jupiter (256) , Zeus (512) , Leto (1024) and Latona (2048) .

maximum of the spectrum decreases as it shifts towards smaller $k_\leftrightarrow$ for Jupiter (256) . Whereas, in Latona (2048) , the global maximum of the final distribution is actually slightly greater than the initial one. This means that more error energy is being transferred to the largest scales in a shorter period of time. The propagation of error is different in figure III.15, instead of a local phenomenon, there is a global propagation of error on the vertical error spectrum that spans rapidly across all possible scales and then dwindles uniformly accordingly to the decaying nature of the experiments. Here, the distance between spectra is practically constant throughout every vertical scale.

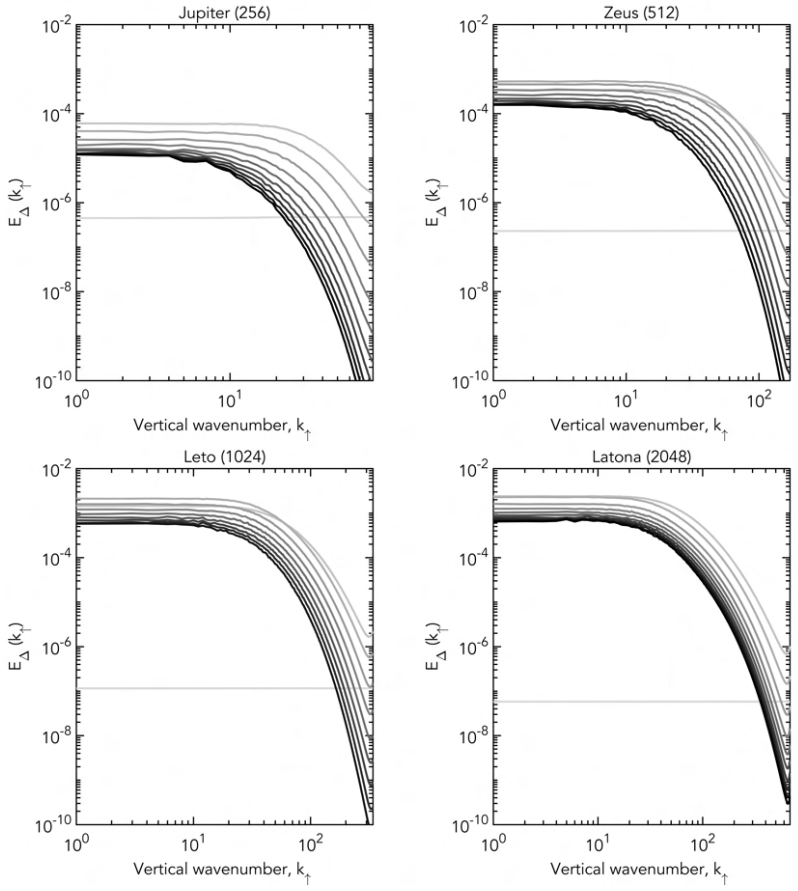

Figure III.15: Vertical error energy spectra of Jupiter (256) , Zeus (512) , Leto (1024) and Latona (2048) .

We can complete the spectral analysis picture once we pass to the ratio energy distribution presented in figure III.16, as this diagnostic allows us to quantify the growth of the relative error normalized by the amount of ensemble kinetic energy. For this quantity, the effects of the buoyancy Reynolds number are most contrasting, as we don't see the exact same story unveiling through the panels. At first glance, the Jupiter (256) behavior is notably different. That is because the error at large wavenumbers has not been able to saturate as in the case of Leto (1024) or even more evidently in the case of Latona (2048) . This aspect is difficult to discern by looking at the ensemble spectra and error spectra

on their own; however, with the ratio spectra we are able to observe the speed at which a wide range of small scales end up decorrelated and the progression of error contaminating neighbouring scales. Even though the relative amount of saturated scales with respect to the total range of wavenumbers grows as Re_b increases, we can recognize that the region dominated mainly by decaying error (which was unable to reach full saturation) is in $10 \lesssim k \lesssim 100$ for all the experiments. Likewise, we can appreciate how the relative error of the largest scales (take $k = 1$ for example) gets gradually bigger. This break down allow us to state that the stratified flows are less predictable as the buoyancy Reynolds number increases.

Proceeding with the horizontal ratio spectra in figure III.17, the predictability trend of the isotropic case is well preserved as expected. Starting with Jupiter (256) , which does not exhibit any horizontal scale with error saturation, there is still a backward propagation of error at small horizontal wavenumber. It seems that the relative error tends to a rather linear distribution instead of a self-similar curve as in the other experiments with higher Re_b.

Moving on to the rest of the experiments, we still can see that there is a wider range of saturated scales in comparison to the isotropic case. In fact, unlike the three dimensional case of error ratio spectra, in figure III.17 the horizontal energy ratio spectra of all the experiments trace a continuous evolution towards larger scales (as smaller scales become completely decorrelated) without any visible *decaying* region. Besides that, all the experiments share qualitatively the same behavior.

Finally, in figure III.18 we present the vertical relative error spectra. Here, as Re_b increases, the final spectrum seems to stay constant at large scales, with a linear distribution for intermediate scales and it ends with the saturation region. Even though the dissipative nature of turbulence plays a leading role on predictability (or the loss of it to be more precise), we can observe that it presents a stronger influence on the vertical scales than in the horizontal ones. Notice that the saturation region is practically entirely defined in the second spectral line, which corresponds to $t = 1$, or around half a turnover time after the birth of the twins.

All of these results are a direct consequence of the characteristic anisotropy presented in stratified flows. Let's resume our discussion from section III.1, regarding the extent of the saturation regions with respect to k, $k_{\leftrightarrow}$ and $k_{\uparrow}$. In

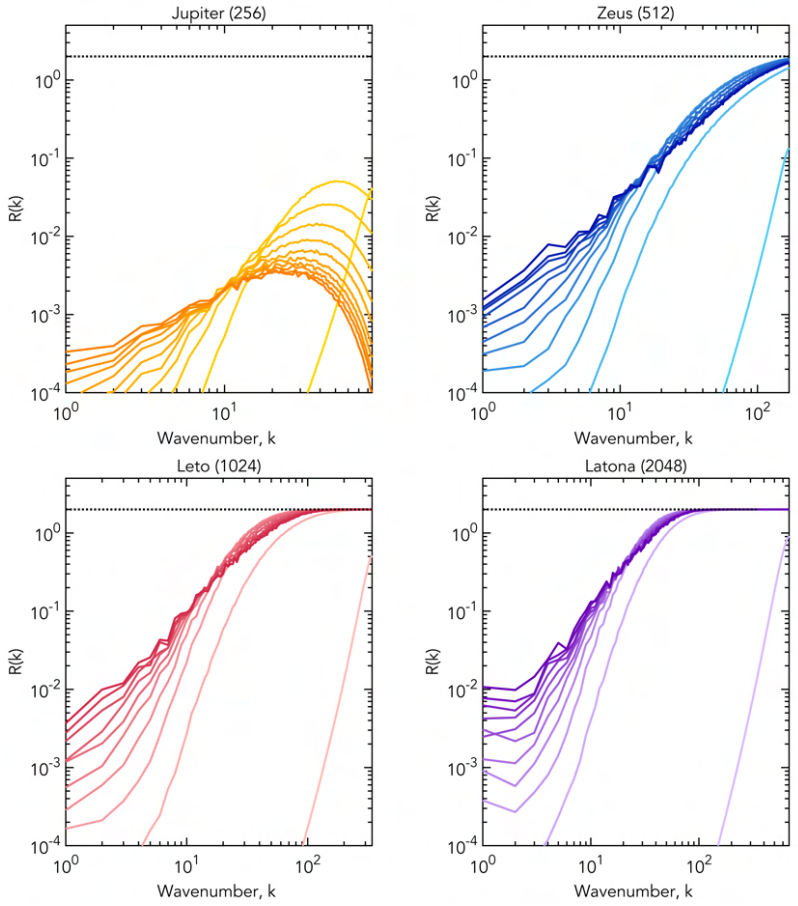

Figure III.16: Error ratio kinetic energy spectra of Jupiter (256) , Zeus (512) , Leto (1024) and Latona (2048) . The spectra are plotted each 0.5 time units from 0.5 to 5.5.

the case of Latona (2048) , structures with $k_{\leftrightarrow} \sim 20$ (where the error starts to saturate) must be associated, because of anisotropy, to larger $k_{\uparrow} \sim 60$ in order to reconcile the outcome of the isotropic wavenumber.

Lastly, we present the time series analysis, starting with figure III.19, which displays the total error kinetic energy for each of the four experiments of this section as a function of time. In that figure, we can observe how the spatial average of the difference energy between fields increases at first and reaches a

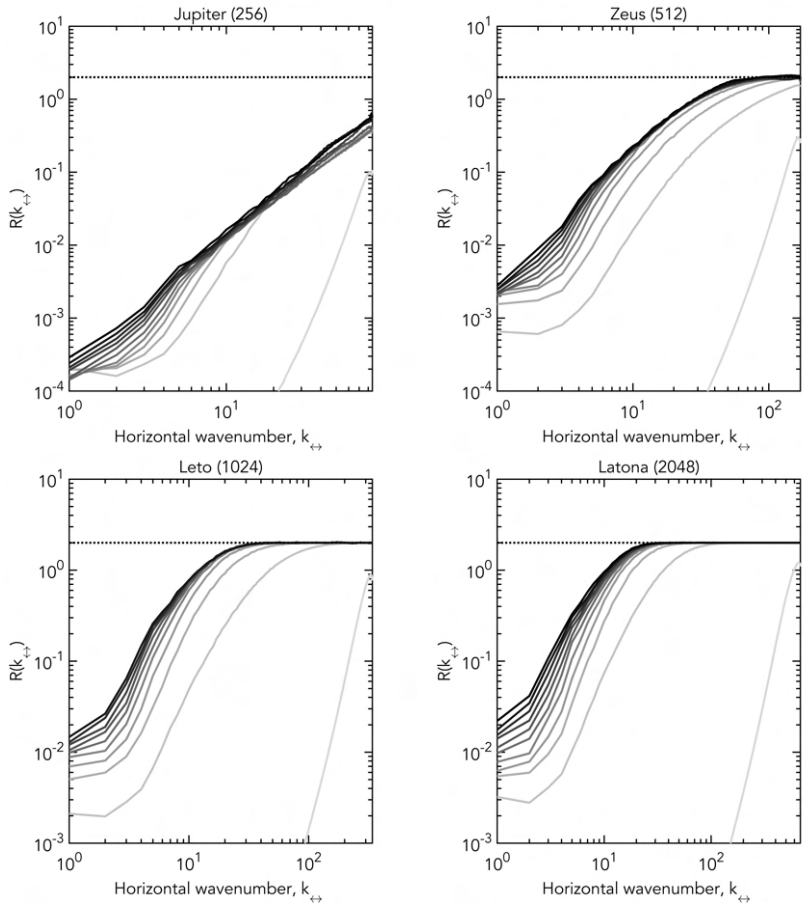

Figure III.17: Horizontal error ratio spectra of Jupiter (256) , Zeus (512) , Leto (1024) and Latona (2048) . The spectra are plotted each 0.5 time units from 0.5 to 5.5.

global maximum. That is a straight consequence of the propagation and saturation of error in general. Notice that the global maxima gets higher and is reached at earlier times as the buoyancy Reynolds number increases. The amplitude increment may be attributed to the wider range of small scales (which saturate faster) existing in the higher resolution experiments; nevertheless, we have to acknowledge that this diagnostic only contains global information, so there is likely a shared contribution across scales. Subsequently, the function decreases as expected given the energy draining feature of decaying turbulence.

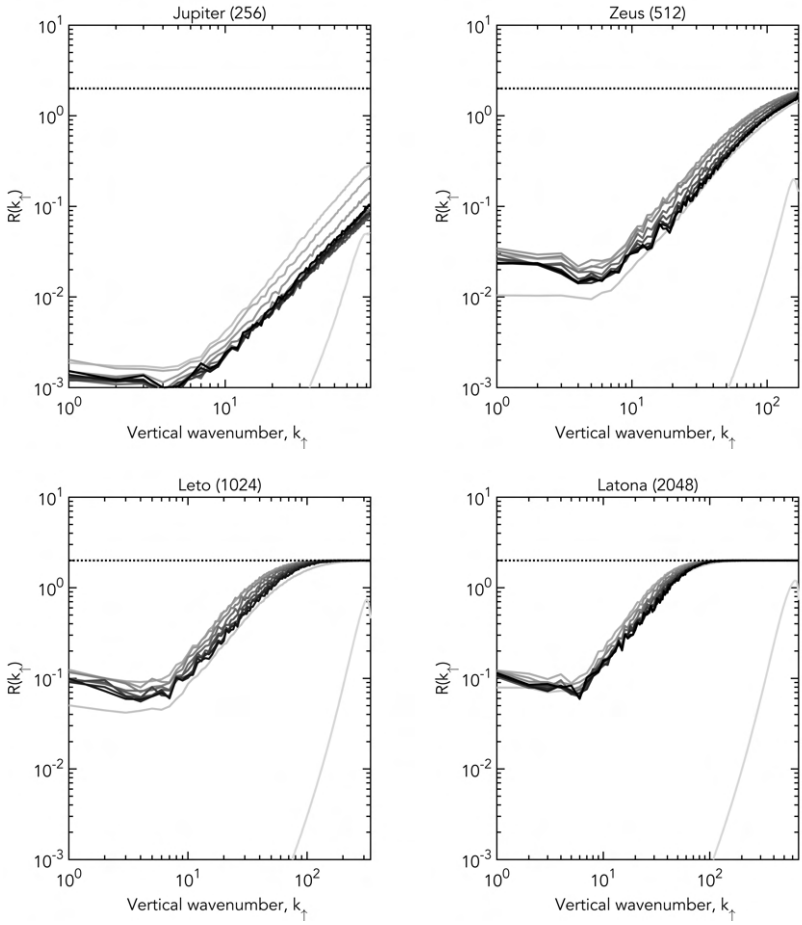

Figure III.18: Vertical energy ratio spectra of Jupiter (256) , Zeus (512) , Leto (1024) and Latona (2048) . The spectra are plotted each 0.5 time units from 0.5 to 5.5.

One important thing to remember looking back at the spectral analysis is that we have a wider range of wavenumbers as simulations grow in resolution (as a result of decreasing the viscosity to increase the Reynolds number), which can represent an inconvenience when trying to directly compare them by eye. For that reason we have in figure III.20 the time series of the relative error $r_K(t)$ at three different scales shared by all experiments which gives us a more detailed picture of what is happening at a local scope. For instance, at the smallest wavenumber $k = 1$, $r_1(t)$ *just* exhibits a steady growth, as the

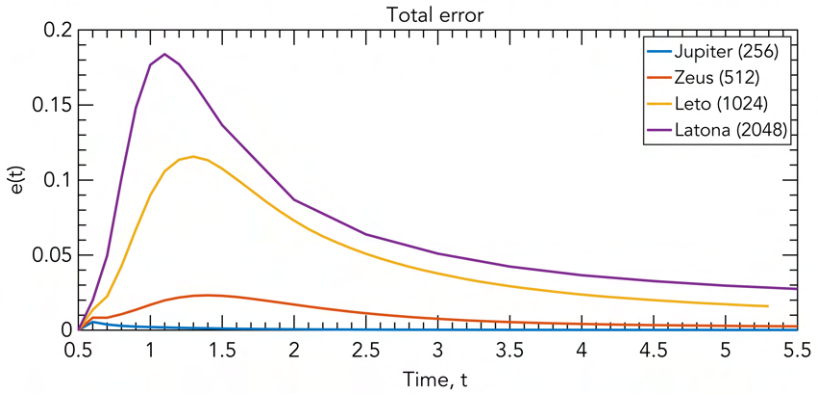

Figure III.19: Total kinetic energy error time series for Jupiter (256) , Zeus (512), Leto (1024) and Latona (2048) .

cumulative result of the backwards error propagation to the largest scales. At $k = 10$, after the initial surge of relative error, we see that the growth of the error ratio stagnate across all the experiments, resulting in a concave function. Going back to figure III.16, it is around this scale where we were able to identify the fore mentioned *balance* scale. The similar shape, but different amplitude between the cases is remarkable, as they present consistent local error dynamics apparently modulated by the amount of total error.

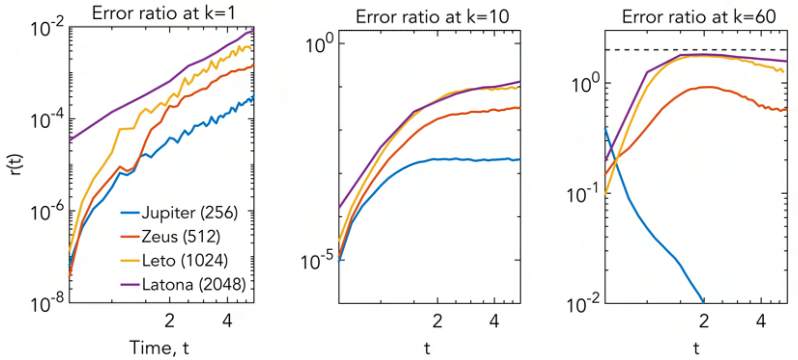

Figure III.20: Relative kinetic energy error as a function of time at a fixed wavenumber for Jupiter (256) , Zeus (512), Leto (1024) and Latona (2048) . From left to right, $k \in \{1, 10, 60\}$.

Finally, at $k = 60$ the error ratio immediately reaches values close to saturation followed by a progressive decrease after approximately one turn-over time. It is important to notice that there is a considerable jump in the behavior of the functions as we go from Zeus (512) to Leto (1024) across the last two panels. On the other hand, it is remarkable how close Leto (1024) and Latona (2048) functions are to one another, even though there is a significant difference in their buoyancy Reynolds numbers and in their total error.

In conclusion, Figure III.20 is an excellent visual summary of the three distinctive regions presented throughout the experiments.

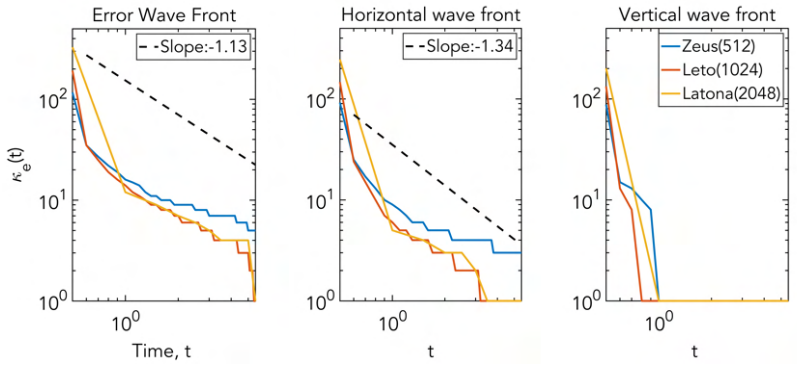

Figure III.21: Isotropic, horizontal and vertical error wave front for Zeus (512), Leto (1024) and Latona (2048) . The reference line is a linear fit of Leto (1024).

At the end of this section, we turn our attention to the cross-over wavenumber or error wavefront in figure III.21, that is the scale at which the error ratio reaches a certain threshold as it propagates towards larger scales. Given that Jupiter (256) is not able to exhibit the full development of an inverse cascade, we only display the diagnostic on Zeus (512) , Leto (1024) and Latona (2048). Both the isotropic and horizontal wavefronts present a negative power law progression with $\kappa_e(t) \sim t^{-1}$, in close agreement with previous studies such as Leith and Kraichnan (1972) and Chollet and Métais (1989). There is no similar behavior for the vertical wavenumbers as the error propagation perish rapidly, which we would expect as there is no inverse cascade of error in vertical wavenumber. Despite having a similar behavior, we can observe how there is a stronger backwards propagation of error for $k_{\leftrightarrow}$ inasmuch as having a steeper slope in comparison with the isotropic wavefront. In fact, the horizontal wave-

front posses a slope closer to the stationary isotropic turbulence studied by Métais and Lesieur (1986) than their decaying case, which could be a direct consequence of the anisotropy of our experiments. We can appreciate that both Leto (1024) and Latona (2048) present a faster propagation compared with Zeus (512) , this mirror our previous discussion indicating that there may exist a phenomenological jump from Zeus (512) to Leto (1024) .

III.2.2 Similar Re_b with different stratification.

In order to have an adequate evaluation of the dependence of the predictability of the stratified turbulence on the buoyancy Reynolds number, it is necessary to compare experiments with similar Re_b obtained alternatively through different parameters. One way to handle this is to change the amount of stratification by changing the buoyancy frequency while maintaining the same viscosity for experiments with same resolution. For this section, we took as base the cases of Zeus (512) and Leto (1024) and only modified their respective buoyancy frequencies to obtain Suez (512) and Otel (1024) . Notice that experiments with the same resolution also share the same Reynolds number. As shown in table II.1, Zeus (512) and Otel (1024) have a comparable buoyancy Reynolds number of $Re_b \sim 4$, while Leto (1024) and Suez (512) feature a $Re_b \sim 11.5$.

For this part, instead of showing the ensemble and error spectra, we will focus on the relative error spectra as it neatly summarizes the information of the previous two. Starting with the isotropic wavenumber spectra, in figure III.22 the error ratio of the aforementioned experiments is exhibited. Even though all the experiments share a similar behavior, there are certain differences that are worth noticing. For example, if we centre our attention on the error saturation, at first sight we can appreciate that experiments with higher Re present a wider range of error saturation. However, we have to remember that they have a wider range of available scales. In fact if we calculate the lowest wavenumber at which there is *full* saturation of error, *i.e.* the first wavenumber k_s such that $R(k_s, t) = 2$, we obtain that Zeus (512) has $k_s = 177$, Otel (1024) has $k_s = 217$, Suez (512) has $k_s = 158$ and Leto (1024) has $k_s = 126$. Which indicates that experiments with similar buoyancy Reynolds are closer with respect to this parameter. Therefore, we still obtain that high Re_b experiments present less predictability altogether. We can analyse the strength of the inverse error cascade by focusing on the impact of the relative error over the large scales (from $k = 1$ to $k = 10$). There is a striking disparity between Otel (1024) and Zeus (512) as the former one differs from the later in almost an order of magnitude. As it is difficult to evaluate the cascade by looking at the spectra, we need to rely on the later displayed time series analysis in order to make further observations.

Furthermore, an interesting remark is that Suez (512) presents a slower propagation of error, which we can see when we compare the space between the first two spectra. In most of the cases the error expands rather quickly and saturates the smallest scales from $t = 0.5$ to $t = 1$. Suez (512) , in contrast, takes a little longer, which may be a consequence of having less stratification.

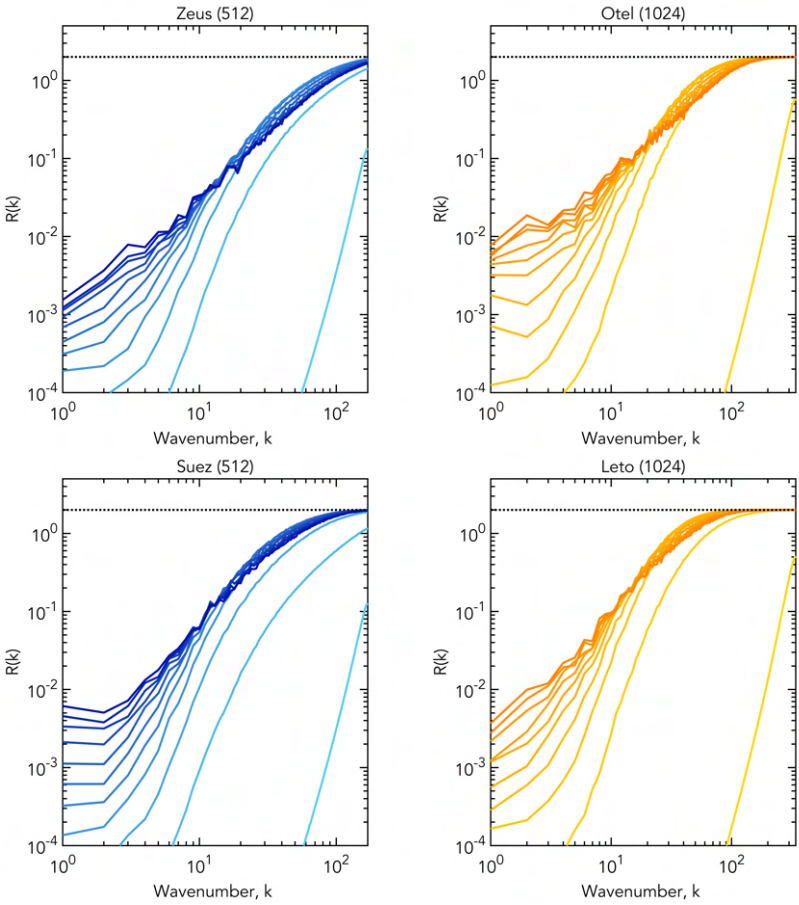

Figure III.22: Error ratio kinetic energy spectra of Zeus (512, $Re_b = 4.6$), Otel (1024, $Re_b = 4.1$), Suez (512, $Re_b = 11.4$), Leto (1024, $Re_b = 12.1$). The spectra are plotted each 0.5 time units from 0.5 to 5.5.

We present the horizontal error ratio spectra in figure III.23. Qualitatively, the experiments with the same Re possess more resemblance than the ones with similar Re_b. For instance, there is an accentuated concentration of spectra

at $k = 1$ in both Zeus (512) and Suez (512) . Likewise, the range of saturated wavenumbers is wider for Leto (1024) and Otel (1024) , starting at $k_{\leftrightarrow_s} = 42$ and $k_{\leftrightarrow_s} = 51$ respectively, while Suez (512) starts at $k_{\leftrightarrow_s} = 68$ and Zeus (512) at $k_{\leftrightarrow_s} = 86$. A similar story unfolds with the vertical ratio spectra

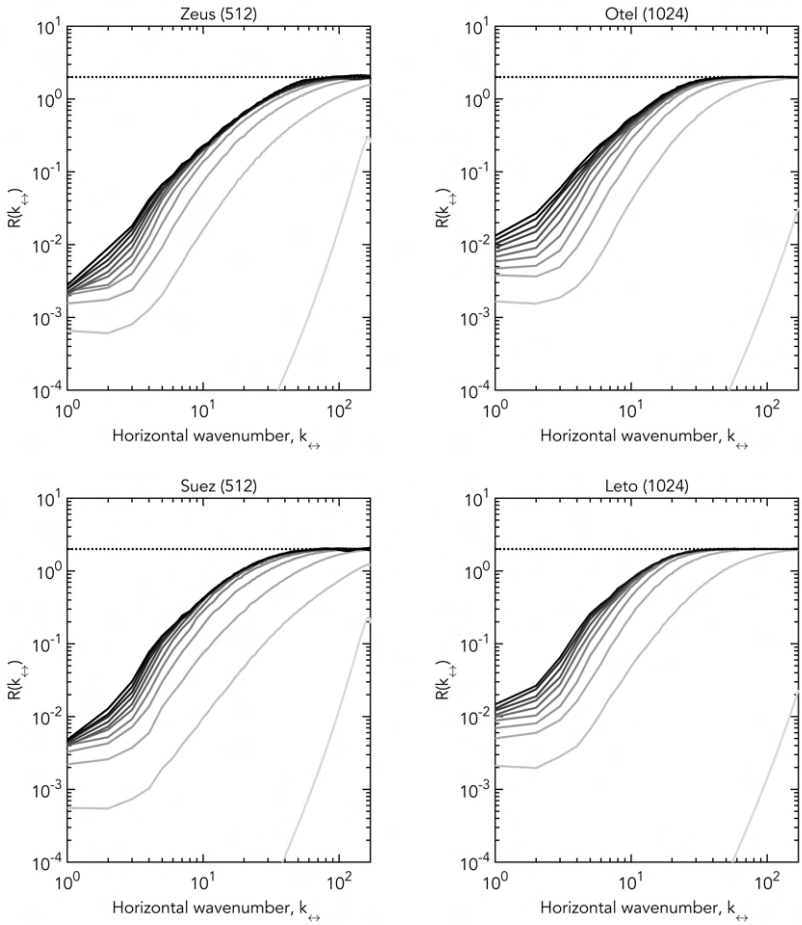

Figure III.23: Horizontal error ratio kinetic energy spectra of Zeus (512) , Otel (1024) , Suez (512) and Leto (1024) . The spectra are plotted each 0.5 time units from 0.5 to 5.5.

(not shown), the spectral evolution of $R(k_\uparrow)$ error is qualitatively unchanged, though the predictability loss is delayed in the case of Suez (512) as well.

Next, we pass to the time series analysis starting with figure III.24. Here, as most of the kinetic energy error is concentrated at large k, the initial growth,

up to the maximum, is due to rapid error saturation at the smallest scales. In section III.2 we concluded that experiments with higher Re_b present a wider range of small scales and, with so, the amplitude of their associated total error grows proportionally.

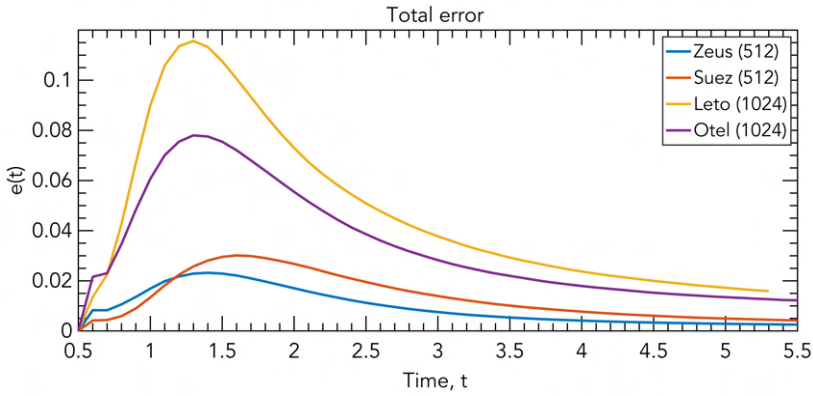

Figure III.24: Total (kinetic energy) error time series for Zeus (512) , Suez (516), Leto (1024) and Otel (1024) .

Having said that, notice that neither Otel (1024) and Leto (1024) nor Zeus (512) and Suez (512) present the same total error maxima. This fact suggests that viscosity plays a significant role in the global error dynamics, since at a fixed Re_b, simulations with larger Re have greater total kinetic energy error. Moreover, Suez (512) reaches its maximum error at a later time than the others, possibly because it has a higher Froude number.

Moving on to the local diagnostics, in figures III.25 and III.26 we display the relative error at a given isotropic and horizontal wavenumber. The selected wavenumbers are representative of small, intermediate and large scale error dynamics. At $k = 1$, where we arguably have at the initial times a positive power law behavior, Otel (1024) exhibits a faster growth, while Suez (512) and Leto (1024) share a closer evolution compared to Zeus (512) . At $k = 10$, the relative error of both Suez (512) and Otel (1024) have a comparable distance to both Zeus (512) and Leto (1024) . At $k = 60$, which is a good reference of the small scale dynamics that saturate and then relaxes as the turbulence decays, the experiments with similar Re_b show greater congruence in their overall development than the ones with same Reynolds number.

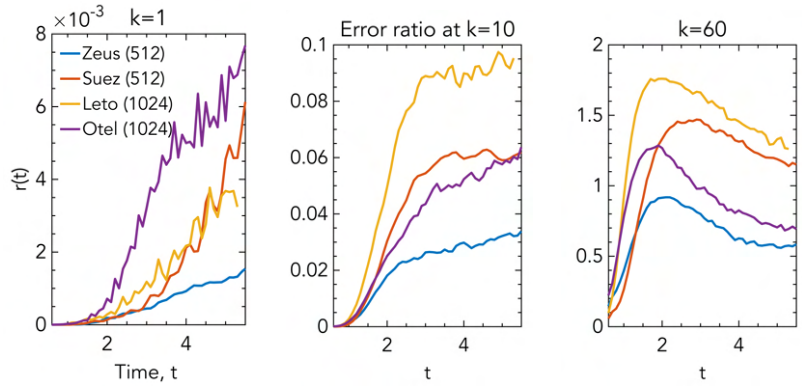

Figure III.25: Relative kinetic energy error as a function of time at a fixed wavenumber for Zeus (512) , Suez (512) , Leto (1024) and Otel (1024). From left to right, $k \in \{1, 10, 60\}$.

Now, at $k_{\leftrightarrow} = 1$ in figure III.26, there is a clear resemblance between the experiments with the same Re: Suez (512) and Zeus (512) present the same modest rate of change, while Otel (1024) and Leto (1024) have a stronger relative error increment. However, at $k_{\leftrightarrow} = 10$ the ratio error of the experiments unfolds on par with the isotropic case at $k = 10$, where there is no clear distinction as to whether Re_b or Re play a more critical role in error dynamics.

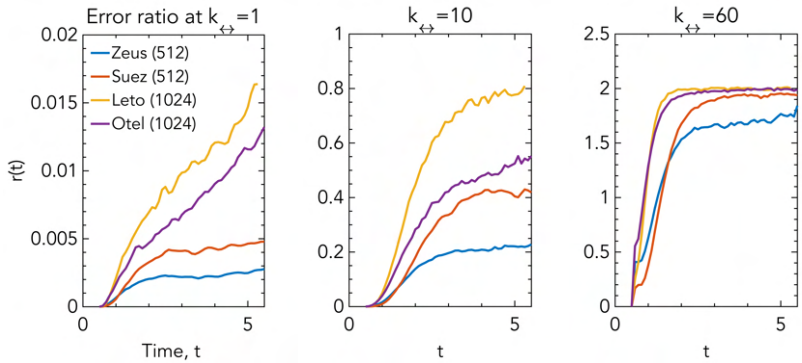

Figure III.26: Relative kinetic energy error as a function of time at a fixed horizontal wavenumber for Zeus (512) , Suez (512) , Leto (1024) and Otel (1024). From left to right, $k_{\leftrightarrow} \in \{1, 10, 60\}$.

At $k_{\leftrightarrow} = 60$ all the experiments are in the near saturation range with Leto (1024) and Otel (1024) displaying closer values with respect to each other. Notice that Leto (1024) presents the highest values in every single panel of III.25 and III.26 with the exception of $k = 1$, becoming in this way the experiment with less predictability. On the other hand, Zeus (512) is consistently the experiment with the highest predictability having the least amount of relative error throughout these comparisons. In summary, at a fixed Re, increasing Re_b via a decrease in stratification results on reduced predictability. Likewise at a fixed Re_b, increasing Re (and decreasing the Froude number) we end up with less predictability as well.

Finally, we have the three dimensional and horizontal error wave front in figure III.27. As expected, Otel (1024) and Suez (512) continue the trend of previous experiments having a negative power law as the rate of error propagation towards larger scales. In both panels, Leto (1024) and Otel (1024) present a slightly steeper slope, which translates into faster error propagation. The error wave front at earlier times differs to its behavior in later times. For example, at the beginning Suez (512) seems to be above all the other graphs, later on Zeus (512) takes that place, which is related with slower rate of error contamination and, consequently, with more predictability.

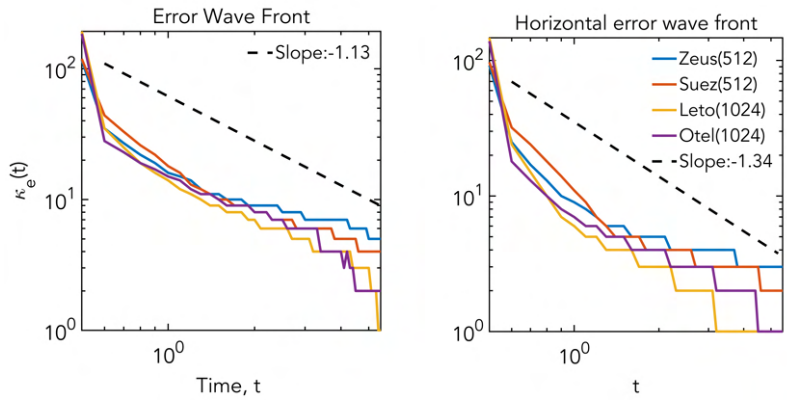

Figure III.27: Isotropic and horizontal error wave front for Zeus (512), Suez (512) , Leto (1024) and Otel (1024) . The reference line is a linear fit of Leto (1024).

III.3 Error introduction

Up to this point, a number of fair questions may have arisen in the reader's mind while avidly perusing the above results and their range of validity under different conditions. In particular, it is a valid concern to wonder *how exactly the specific choice of noise addition may influence the final outcome of the numerical experiments?* In any predictability study, the implications of this issue are crucial, as they provide robustness and generality to the results. This final section is concerned with dissecting that question and providing a reply to some of the natural inquiries related with error introduction. For instance, all the experiments in section III.2 have shared the same wavenumber error cutoff at $k_c = 20$, while changing the amplitude of the random perturbations accordingly so that all experiments roughly share the same amount of initial error. In the stratified turbulence realm this could have great significance given the existence of a transitional scale such as the Ozmidov wavenumber. It may be the case that the error dynamics present some kind of conversion if the cutoff wavenumber is placed behind or ahead of that threshold.

III.3.1 Wavenumber cutoff dependency

Let's start exploring the sensitivity of the predictability results with respect to the wavenumber cutoff selection. Our approach is fairly simple, taking the base experiment, Leto (1024) , and selecting a different cutoff wavenumber $k_c \in \{20, 40, 60, 80\}$[2], while still keeping the same amount of total initial error and the same fluid variables such as stratification, viscosity, etc. In figure III.28 we have the error spectra using the aforementioned cutoff wavenumbers. At a first sight, the reader may be wondering if his/her eyes are seeing the exact same figure repeated across the panels. However, we can appreciate how the initial error spectrum (accentuated in a different color) effectively distinguishes each experiment. Note that the characteristic step function changes in height as a mere consequence of the condition of having the same total initial error. Besides that initial spectral line, the strong resemblance of the following spectra is uncanny. This fact lead us to figure III.29, which shows the error ratio spectra. Instead, we obtain an identical story, the highlighted initial spectra in III.29 is

[2] An important remark is that we keep the same unperturbed twin (Apollo) for all the following experiments, and we just run modified versions of Artemis.

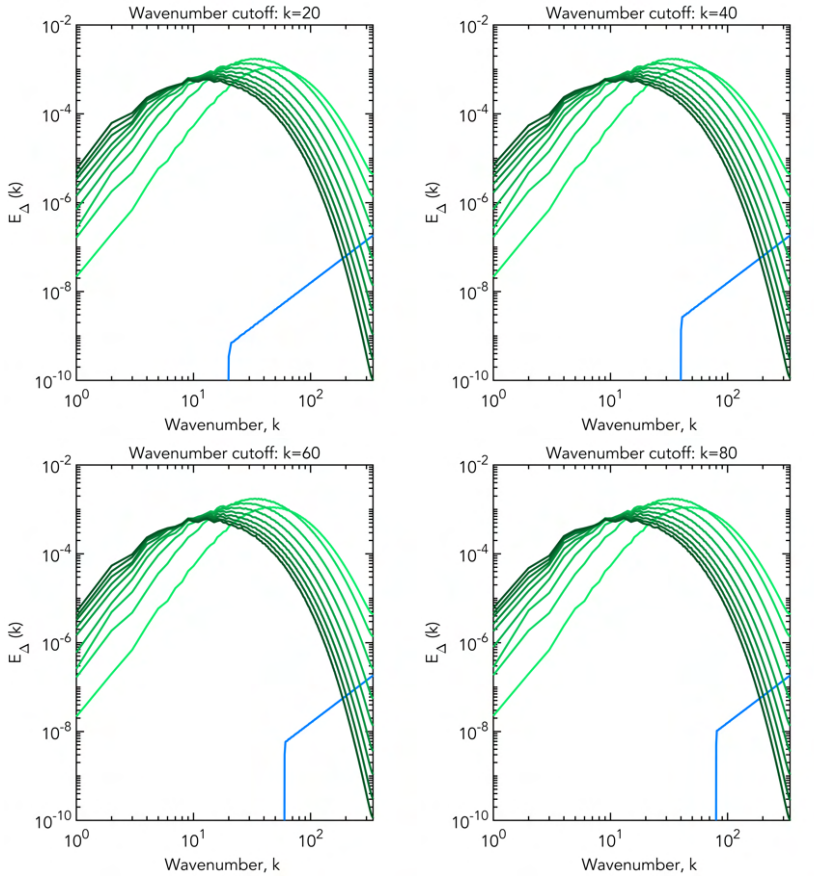

Figure III.28: Error energy spectra of the modified Leto (1024) experiment with cutoff wavenumbers at $k = 20, 40, 60, 80$. The initial error spectrum is highlighted in blue.

the only distinctively different and the rest of the spectra are virtually the same. We have omitted the horizontal and vertical decomposition of the error and ratio spectra, as the nearly indistinguishable tendency continues within the spectral analysis of this quantities as well. Conversely, it is worth remembering that the Ozmidov wavenumber for these experiments takes a value of $k_O = 50$ and there is no discernible change at either of the spectral diagnostics when we sweep the cutoff wavenumber through that value.

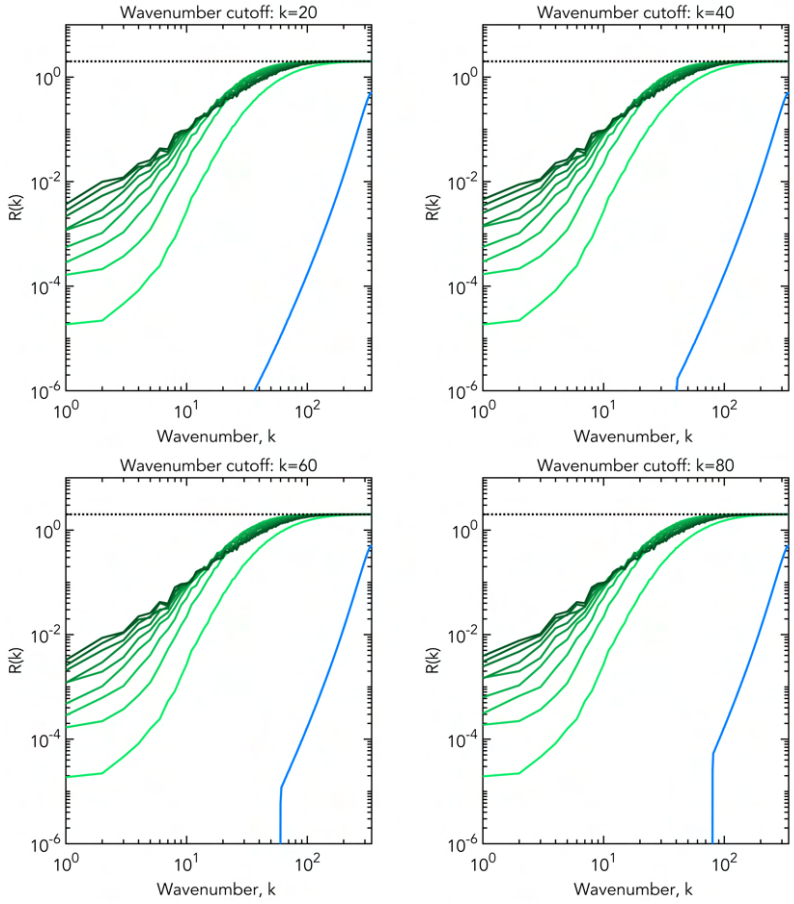

Figure III.29: Ratio energy spectra of the modified Leto (1024) experiment with cutoff wavenumbers at $k = 20, 40, 60, 80$. The initial ratio spectrum is highlighted in blue.

Moving on, in figure III.30 we present the total error and error wavefront time series. As the figures almost speak for themselves, the total error of each experiments ends up being identical again, as is the case with the error wavefront. This is quite remarkable, as they provide the conclusion that both on the local and global scale, the experiments undeniably share the same error propagation characteristics.

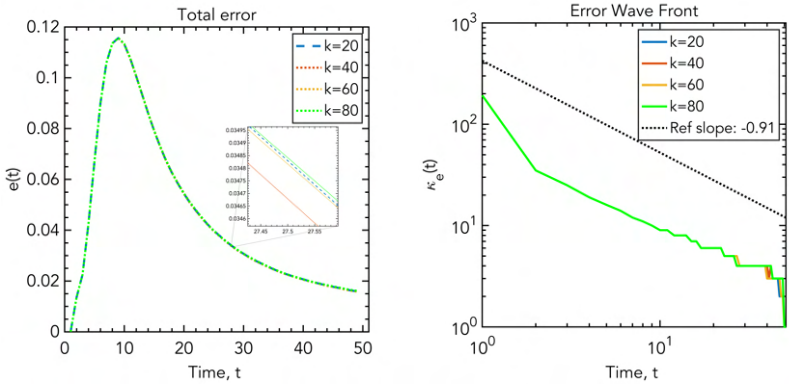

Figure III.30: Time series of the total error and error wavefront for the modified Leto (1024) experiment with cutoff wavenumbers at $k = 20, 40, 60, 80$.

The overall conclusion is straightforward: there is no correlation or dependency whatsoever between the studied range of cutoff wavenumbers and the final outcome of the experiments. One is definitely tempted to push a little further the studied range, insomuch as to know what would be the consequences of inserting the perturbations at the region mostly characterized by the inverse cascade of error (setting $k_c \sim 10$ for instance).

III.3.2 Geometrical implications: Cylinder v. Sphere

Another legitimate question corresponds to the geometrical nature of the error introduction. Our numerical experiments add random noise with a pre-established amplitude for all wavenumbers beyond the cutoff wavenumber (k_c). This means that we are uniformly adding random perturbations to the velocity field at each grid-point of our cubic Fourier domain outside the sphere of radius k_c, which is reasonable given the isotropic initial conditions but presents a clear asymmetry when dealing with stratified turbulence. Now, it is natural to ponder whether this geometry can expressively alter the amount of error that is injected into each level of what would later become the layered structure. This inquiry leads us to present another modification to our base case, changing the geometry of the error introduction from the complement of a sphere, to the complement of a cylinder while modifying the noise amplitude in order to keep the same total initial error as our reference experiment. In that way, all the horizontal planes in the wave vector domain are supplied with approximately the same amount of initial error.

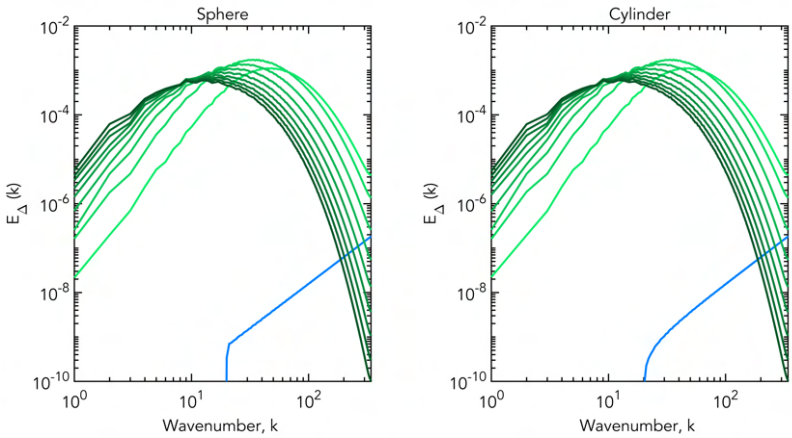

Figure III.31: Error energy spectra of Leto (1024) with spherical and cylindrical complement error addition. The initial error spectrum is highlighted in blue.

The error energy spectra presented in figure III.31 shows us the first comparison between the spherical and cylindrical complement error introduction. Similarly to the case of the modified cutoff wavenumbers in subsection III.3.1, we

see that the spectra maintain almost identical similarity at all times except the initial error spectrum. As highlighted in blue, the initial spectrum of the cylindrical case presents a smoother step function but notice that both curves visibly encapsulate a similar area. In figure III.32 we have the horizontal wavenumber

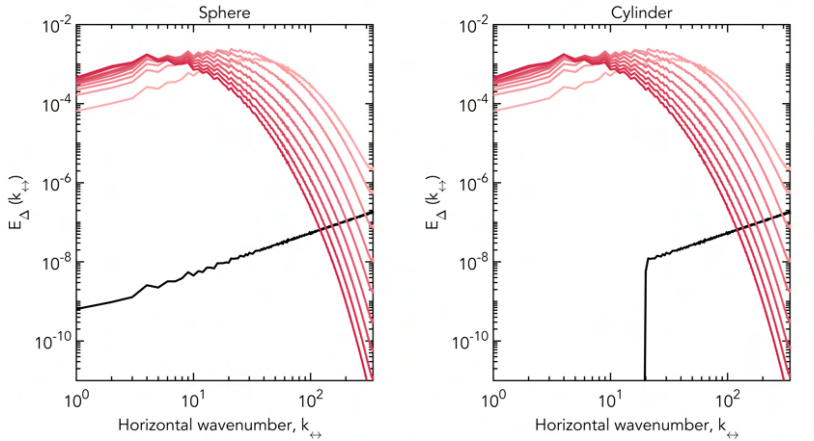

Figure III.32: Horizontal error energy spectra of Leto (1024) with spherical and cylindrical complement error addition. The initial error spectrum is highlighted in black.

spectra of error energy, which effectively shows that there is a uniform amount of initial error insertion at each horizontal plane. In the spherical case we have a continuous and linear initial spectrum as discussed in section III.1, while in the cylindrical case we observe a step function as there is no error contribution at any $k_\leftrightarrow < 20$. Regardless, we obtain a similar result in every subsequent spectrum. For the vertical error spectra, even the initial spectrum is indistinguishable. The ratio error spectra were calculated accordingly, but they are not displayed due to its inability to add something different to this discussion. We still present III.33 to complete the picture that both at the local and global scales, the experiments present the same error growth characteristics. There is no visible dependence on the geometry of the error introduction both on the total error time series nor in the error wavefront.

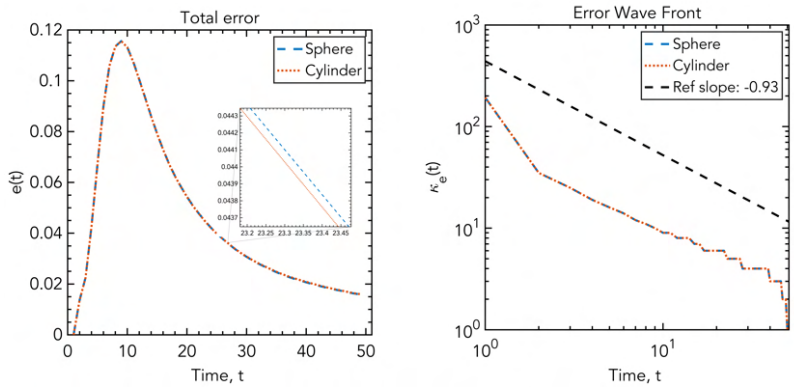

Figure III.33: Total error and error wavefront time series of Leto (1024) with spherical and cylindrical complement error addition.

In summary, the overall results presented in this section strongly suggest that the total amount of error likely carries a more significant weight in the error dynamics compared to the geometrical implications of error introduction and wavenumber cutoff.

Chapter IV

Conclusions

Predictability studies have been built upon Lorenz's original scheme since its conception and they have been developed to analyse predictability on a wide variety of fluid systems. Such a framework establishes that there are certain systems that posses an intrinsic range of predictability which cannot be further extended by reducing the initial error of observation. In those cases, errors at the smallest scales of motion lead to a progressive error propagation toward larger scales in what it is commonly referred to as an inverse cascade of error. The existence of this inverse cascade is closely related with the slope of the kinetic energy spectrum exhibited by the system. Now, given the natural anisotropy of stratified turbulence and its characteristic to present different slopes for the isotropic and horizontal kinetic energy spectrum at different buoyancy Reynolds numbers, there is an opportunity to expand the classical predictability picture to this particular type of turbulence.

Near-identical twin simulations were carried to study in detail the effects of the buoyancy Reynolds number on the predictability of decaying stratified turbulence. Our simulations qualitatively display the vortical layered structures (pancake blovs) associated with stratified turbulence. Similarly, we have been able to show that the energy spectra in such systems, appear to be approaching $k_{\leftrightarrow}^{-5/3}$ as Re_b increases while analysing the slope of the ensemble spectrum at the time of maximum dissipation. The horizontal ensemble spectrum arguably presents as well a power law cascade of kinetic energy, which does not occur in the case of vertical wavenumbers.

Moving on to predictability diagnostics, we were able to determine the existence of an inverse cascade of error on both the isotropic and horizontal wavenumbers with the analysis of the error kinetic energy spectra. Both of these cases present two characteristic regions: at large physical scales the error spectrum development is dominated by the inverse cascade of error, while at intermediate scales the decaying nature of the system takes a major role. We postulated the existence of a particular scale which denotes the balance between both regions and whose location barely changes with respect to Re_b.

Furthermore, we qualitatively corroborated the *self-similar* evolution of the error spectra. Without a doubt the self-similar nature of the energy cascade yields a self-similar error spectra. However there is a clear distinction between the local error dynamics on the vertical scales. For this case, the error is propagated uniformly across all possible scales without the existence of a local (and gradual) contamination of error towards larger scales.

The error ratio spectra shows another striking feature within the predictability frame, which is the range of wavenumbers with error saturation (with complete decorrelation between velocity fields). This feature is shared for the isotropic, horizontal and vertical spectra regardless of the existence of the inverse cascade of error and extends to a wider range of scales as we increase the buoyancy Reynolds number. At the smallest k there is an exponential growth of error.

We can quantify the scale at which the error is propagating via the error wavefront. This diagnostic showed that both the isotropic and horizontal wavefronts presented a negative power law progression $\kappa_e(t) \sim t^{-1}$, in close agreement with previous scaling studies. Likewise, experiments with higher Re_b displayed faster rate of error propagation. The overall conclusion of the experiments with same stratification is that predictability is reduced with respect to higher buoyancy Reynolds number.

Moving on to the section with similar Re_b with different stratification, we observed that Re also plays a significant role in predictability of stratified flows. Some key diagnostics tip the balance towards Re being a more significant parameter as simulations with same Re have a closer resemblance both in the isotropic and horizontal ratio spectra. Nonetheless, our results suggest that the predictability picture is more complex. There is a multi-factor dependency which cannot be restricted solely to the buoyancy Reynolds number or to

Re by itself. As a general conclusion for this part, we obtained that at a fixed Re, increasing Re_b via a reduction on the stratification results in reduced predictability. On the other hand at a fixed Re_b, increasing Re and increasing the stratification ended up with less associated predictability as well.

A noteworthy result was the repeated independence that presented the experimental outcomes with respect to the diversification of error introduction. We noted how the behavior of the system and its error dynamics are impervious to changing the cutoff wavenumber at which the error is introduced when the initial error kinetic energy is the same. An important remark is that this type of error introduction could be considered a bit artificial, as in closer to real life scenarios, the addition of error from observations is shared throughout all the spectrum and the amplitude of such perturbation may not be uniform as well.

Moreover, there were no discernible changes on the results of the experiments when we modify the geometry of said error introduction from the domain complement of a sphere to the domain complement of a cylinder. The propagation of error stayed the same at both local and global diagnostics. These results point to the fact that the total amount of initial error possess greater importance than the explored caveats of error introduction.

Some of the considerations that may be worth pursuing for future work in this particular line of research would be:

- To extend the same scheme to forced stratified turbulence in order to further analyse the effects of the buoyancy Reynolds number under stationary conditions. This would remove the decay phase and allow us to ultimately achieve saturation of error at the largest scales.

- To explore different regimes of stratification with a fixed Re, in that way we can broaden the conclusions of predictability dependency with respect to Re and Re_b

- To consider more variants of errors introduction such as anisotropical perturbations or addition of colored noise. For instance, the application of Ornstein–Uhlenbeck process as perturbations to the velocity fields could exhibit interesting and more realistic implications.

References

G. K. Batchelor. *The Theory of Homogeneous Turbulence*. Cambridge University Press, 1st edition, 1953.

P. Billant and J.-M. Chomaz. Experimental evidence for a new instability of a vertical columnar vortex pair in a strongly stratified fluid. *J. Fluid Mech.*, 418:167–188, 2000a.

P. Billant and J.-M. Chomaz. Theoretical analysis of the zigzag instability of a vertical columnar vortex pair in a strongly stratified fluid. *J. Fluid Mech.*, 419:29–63, 2000b.

P. Billant and J.-M. Chomaz. Self-similarity of strongly stratified inviscid flows. *Phys. Fluids*, 13:1645–1651, 2001.

G. Boffetta and S. Musacchio. Predictability of the inverse energy cascade in 2d turbulence. *Physics of Fluids*, 13(4):1060–1062, 2001.

G. Boffetta and S. Musacchio. Chaos and predictability of homogeneous-isotropic turbulence. *Phys. Rev. Lett.*, 119, 2017.

G. Brethouwer, P. Billant, E. Lindborg, and J.-M. Chomaz. Scaling analysis and simulation of strongly stratified turbulent flows. *J. Fluid Mech.*, 585: 343–368, 2007.

J.-P. Chollet and O. Métais. Predictability of three dimensional turbulence in large eddy simulation. *Eur. J. Mech. B/Fluids*, 8:523–548, 1989.

P. A. Davidson. *Turbulence: An Introduction for Scientists and Engineering*. Oxford University Press, 2004.

P. A. Davidson. *Turbulence in Rotating, Stratified and Electrically Conducting Fluids*. Cambridge University Press, 2013.

D. R. Durran. *Numerical Methods For Fluid Dynamics With Applications To Geophysics.* Springer, 2nd edition, 2010.

D. R. Durran and M. Gingrich. Atmospheric predictability: Why butterflies are not of practical importance. *Journal of the Atmospheric Sciences*, 71(7): 2476 – 2488, 2014.

K. S. Gage. A climatology of atmospheric wavenumber spectra of wind and temperature observed by commercial aircraft. *J. Atmos. Sci*, 42:950–960, 1985.

J. R. Herring, J. J. Riley, G. S. Patterson, and R. H. Kraichnan. Growth of uncertainty in decaying isotropic turbulence. *Journal of Atmospheric Sciences*, 30(6), 1973.

Y. Kimura and J. R. Herring. Diffusion in stably stratified turbulence. *Journal of Fluid Mechanics*, 328:253–269, 1996.

Y. Kimura and J. R. Herring. Energy spectra of stably stratified turbulence. *Journal of Fluid Mechanics*, 698:19–50, 2012.

A. N. Kolmogorov. The local structure of turbulence in incompressible viscous fluid for very large Reynolds number. *Dok. Akad. Nauk. SSSR*, 30: 301–305, 1941.

R. H. Kraichnan. Inertial ranges in two-dimensional turbulence. *Phys. Fluids*, 10:1417–1423, 1967.

P. K. Kundu and I. M. Cohen. *Fluid Mechanics*. Academic Press, 2nd edition, 2002.

L. D. Landau. On the problem of turbulence. In *Dokl. Akad. Nauk USSR*, volume 44, page 311, 1944.

J. D. Legaspi and M. L. Waite. Prandtl number dependence of stratified turbulence. *Journal of Fluid Mechanics*, 903:A12, 2020. doi: 10.1017/jfm.2020.619.

C. E. Leith. Atmospheric predictability and two-dimensional turbulence. *Journal of the Atmospheric Sciences*, 28:145–161, 1971.

C. E. Leith and R. H. Kraichnan. Predictability of turbulent flows. *Journal of Atmospheric Sciences*, 29(6):1041 – 1058, 1972.

M. Lesieur. *Turbulence in Fluids*. Springer, 4th edition, 2014.

D. K. Lilly. Numerical simulation studies of two-dimensional turbulence: Ii. stability and predictability studies. *Geophysical Fluid Dynamics*, 4(1):1–28, 1972.

D. K. Lilly. Stratified turbulence and the mesoscale variability of the atmosphere. *J. Atmos. Sci.*, 40:749–761, 1983.

J. T. Lin and Y. H. Pao. Wakes in stratified fluids: A review. *Annu. Rev. Fluid Mech.*, 11:317–338, 1979.

E. Lindborg. The energy cascade in a strongly stratified fluid. *Journal of Fluid Mechanics*, 550:207–242, 2006.

E. N. Lorenz. The predictability of a flow which possesses many scales of motion. *Tellus*, 21(3):289–307, 1969.

T. S. Lundgren. Kolmogorov turbulence by matched asymptotic expansions. *Physics of Fluids*, 15(4):1074–1081, 2003.

P. Lynch. *The Emergence of Numerical Weather Prediction: Richardson's Dream*. Cambridge University Press, 2006.

A. Maffioli and P. A. Davidson. Dynamics of stratified turbulence decaying from a high buoyancy Reynolds number. *J. Fluid Mech.*, 786:210–233, 2016.

W. D. McComb. *The Physics of Fluid Turbulence*. Oxford University Press Inc., 1990.

R. E. Morss, C. Snyder, and R. Rotunno. Spectra, Spatial Scales, and Predictability in a Quasigeostrophic Model. *Journal of Atmospheric Sciences*, 66(10), 2009.

O. Métais and M. Lesieur. Statistical predictability of decaying turbulence. *Journal of Atmospheric Sciences*, 43(9):857 – 870, 1986.

K. Ngan, P. Bartello, and D. N. Straub. Predictability of rotating stratified turbulence. *Journal of the Atmospheric Sciences*, 66(5), 2009.

S. A. Orszag. Analytical theories of turbulence. *Journal of Fluid Mechanics*, 41:363–386, 1970.

R. V. Ozmidov. On the turbulent exchange in a stably stratified ocean. *Izvestia Akad. Nauk. SSSR Atmospheric and Oceanic Physics Ser.*, 1:853–860, 1965.

O. Reynolds. An experimental investigation of the circumstances which determine whether the motion of water shall be direct or sinuous, and of the law of resistance in parallel channels. *Philosophical Transactions of the Royal Society*, 174:935–982, 1883.

L. F. Richardson. *Weather Prediction by Numerical Process*. Cambridge University Press, 1922.

J. J. Riley and S. M. deBruynKops. Dynamics of turbulence strongly influenced by buoyancy. *Phys. Fluids*, 15:2047–2059, 2003.

J. J. Riley and M.-P. Lelong. Fluid motions in the presence of strong stable stratification. *Annu. Rev. Fluid Mech.*, 32:613–657, 2000.

J. J. Riley and E. Lindborg. Stratified turbulence: A possible interpretation of some geophysical turbulence measurements. *J. Atmos. Sci.*, 65:2416–2424, 2008.

J. J. Riley and E. Lindborg. Recent progress in stratified turbulence. In *Ten Chapters in Turbulence*, pages 269–317. Cambridge University Press, 2012.

R. Rotunno and C. Snyder. A generalization of lorenz's model for the predictability of flows with many scales of motion. *Journal of the Atmospheric Sciences*, 65(3):1063 – 1076, 2008.

S. G. Saddoughi and S. V. Veeravalli. Local isotropy in turbulent boundary layers at high reynolds number. *Journal of Fluid Mechanics*, 268:333–372, 1994.

L. M. Smith and F. Waleffe. Generation of slow large scales in forced rotating stratified turbulence. *Journal of Fluid Mechanics*, 451:145–168, 2002.

G. I. Taylor. Statistical theory of turbulence. *Proc. R. Soc. London, Ser. A*, 151: 421–444, 1935.

P. D. Thompson. Uncertainty of initial state as a factor in the predictability of large scale atmospheric flow patterns. *Tellus*, 9(3):275–295, 1957.

J. J. Tribbia and D. P. Baumhefner. Scale interactions and atmospheric predictability: An updated perspective. *Monthly Weather Review*, 132(3), 2004.

M. L. Waite. Stratified turbulence at the buoyancy scale. *Physics of Fluids*, 23 (6), 06 2011.

M. L. Waite. Direct numerical simulations of laboratory-scale stratified turbulence. In T. von Larcher and P. D. Williams, editors, *Modelling Atmospheric and Oceanic Flows: Insights from Laboratory Experiments and Numerical Simulations*, pages 159–175. American Geophysical Union, 2014.

M. L. Waite and P. Bartello. Stratified turbulence dominated by vortical motion. *J. Fluid Mech.*, 517:281–308, 2004.

K. Yoshimatsu and T. Ariki. Error growth in three-dimensional homogeneous turbulence. *Journal of the Physical Society of Japan*, 88(12):124401, 2019.